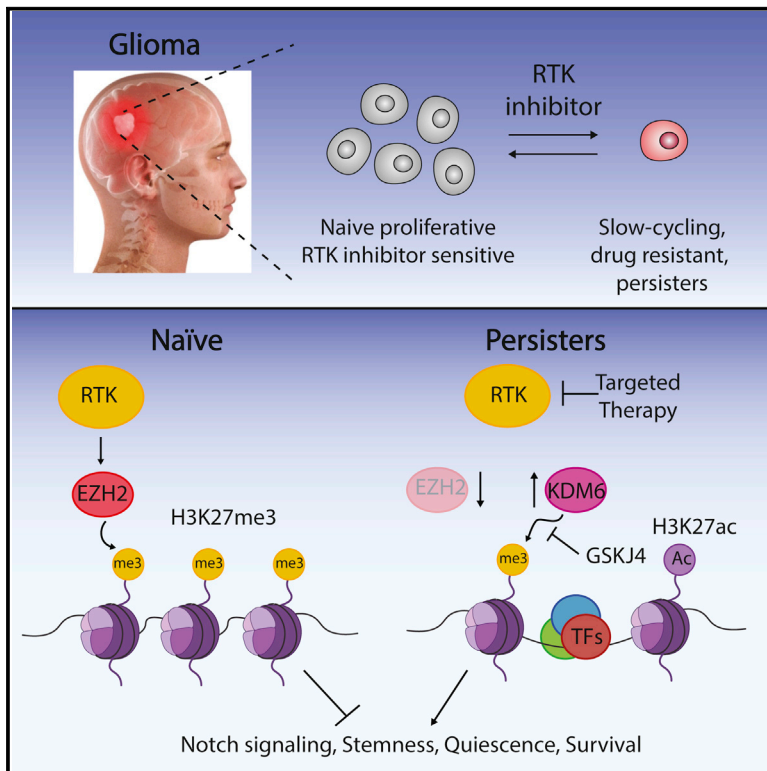


Cell Stem Cell

Adaptive Chromatin Remodeling Drives Glioblastoma Stem Cell Plasticity and Drug Tolerance

Graphical Abstract



Authors

Brian B. Liao, Cem Sievers,
Laura K. Donohue, ..., Mario L. Suvà,
Anoop P. Patel, Bradley E. Bernstein

Correspondence

apatel1@uw.edu (A.P.P.),
bernstein.bradley@mgh.harvard.edu
(B.E.B.)

In Brief

Liao et al. find that glioblastoma stem cells (GSCs) reversibly transition to a slow-cycling, persister-like state following RTK inhibitor treatment. The persister state is marked by redistribution of repressive chromatin, upregulation of neurodevelopmental programs, and dependency on KDM6. Thus, cancer cells may hijack chromatin reorganization for proliferation, adaptation, and tolerance.

Highlights

- GSCs can become drug-tolerant and persister-like following RTK inhibitor exposure
- Persister GSCs exhibit NSC-like programs and are sustained by Notch signaling
- Notch-high, slow-cycling GSCs are found in primary GBM tumors
- Persister GSCs reorganize their repressive chromatin and are dependent on KDM6



Adaptive Chromatin Remodeling Drives Glioblastoma Stem Cell Plasticity and Drug Tolerance

Brian B. Liao,^{1,2,7} Cem Sievers,^{1,2,7} Laura K. Donohue,^{1,2} Shawn M. Gillespie,^{1,2} William A. Flavahan,^{1,2} Tyler E. Miller,^{5,6} Andrew S. Venteicher,^{1,2,3} Christine H. Hebert,^{1,2} Christopher D. Carey,⁴ Scott J. Rodig,⁴ Sarah J. Shareef,^{1,2} Fadi J. Najm,^{1,2} Peter van Galen,^{1,2} Hiroaki Wakimoto,³ Daniel P. Cahill,³ Jeremy N. Rich,^{5,6} Jon C. Aster,⁴ Mario L. Suvà,^{1,2} Anoop P. Patel,^{1,2,3,*} and Bradley E. Bernstein^{1,2,8,*}

¹Department of Pathology and Center for Cancer Research, Massachusetts General Hospital and Harvard Medical School, Boston, MA 02114, USA

²Broad Institute of Harvard and MIT, Cambridge, MA 02142, USA

³Department of Neurosurgery, Massachusetts General Hospital and Harvard Medical School, Boston, MA 02114, USA

⁴Department of Pathology, Brigham and Women's Hospital and Harvard Medical School, Boston, MA 02114, USA

⁵Department of Stem Cell Biology and Regenerative Medicine, Lerner Research Institute, Cleveland Clinic, Cleveland, OH 44195, USA

⁶Department of Molecular Medicine, Cleveland Clinic Lerner College of Medicine, Case Western Reserve University, Cleveland, OH 44195, USA

⁷Co-first author

⁸Lead Contact

*Correspondence: apatel1@uw.edu (A.P.P.), bernstein.bradley@mgh.harvard.edu (B.E.B.)

<http://dx.doi.org/10.1016/j.stem.2016.11.003>

SUMMARY

Glioblastoma, the most common and aggressive malignant brain tumor, is propagated by stem-like cancer cells refractory to existing therapies. Understanding the molecular mechanisms that control glioblastoma stem cell (GSC) proliferation and drug resistance may reveal opportunities for therapeutic interventions. Here we show that GSCs can reversibly transition to a slow-cycling, persistent state in response to targeted kinase inhibitors. In this state, GSCs upregulate primitive developmental programs and are dependent upon Notch signaling. This transition is accompanied by widespread redistribution of repressive histone methylation. Accordingly, persisting GSCs upregulate, and are dependent on, the histone demethylases KDM6A/B. Slow-cycling cells with high Notch activity and histone demethylase expression are present in primary glioblastomas before treatment, potentially contributing to relapse. Our findings illustrate how cancer cells may hijack aspects of native developmental programs for deranged proliferation, adaptation, and tolerance. They also suggest strategies for eliminating refractory tumor cells by targeting epigenetic and developmental pathways.

INTRODUCTION

Glioblastoma (GBM), isocitrate dehydrogenase (IDH) wild-type, is the most frequent malignant primary brain tumor. Despite surgical resection, ionizing radiation, and chemotherapy, median survival remains less than 15 months (Tanaka et al., 2013). Cancer genome sequencing has cataloged a spectrum of

genetic alterations in GBM (Brennan et al., 2013; McLendon et al., 2008) and identified potential “druggable” targets. Receptor tyrosine kinases (RTKs) are the most commonly altered genes, with ~67% of adult GBMs harboring alterations of *EGFR* (57%), *PDGFRA* (13%), *MET* (2%), *FGFR2/3* (3%), or other RTKs. *RTK inhibitors have revolutionized treatment for certain cancer types with RTK alterations but have failed to improve overall survival in GBM* (Tanaka et al., 2013).

Therapeutic resistance and relapse in GBM relates to the extensive intratumoral genetic and phenotypic heterogeneity characteristic of these tumors (Eder and Kalman, 2014; Lathia et al., 2015). Evidence indicates that a subpopulation of stem-like cells, termed GBM stem cells (GSCs), underlies tumor propagation, drug resistance, and relapse (Bao et al., 2006; Lathia et al., 2015; Singh et al., 2004). The existence and functional importance of GSCs is supported by in vivo and in vitro evidence. First, a subpopulation of cells with stemness markers is present in human GBM and is enriched upon treatment (Tamura et al., 2013). Second, primary tumor cells expressing stemness markers are highly tumorigenic when orthotopically xenotransplanted into mice (Singh et al., 2004). Third, stem-like cultures established from human tumors in serum-free conditions can propagate tumors and have multipotent differentiation potential (Lee et al., 2006; Singh et al., 2004). GSCs are thus a critical model for the cancer stem cell field (Lathia et al., 2015).

Studies of gene regulatory circuits identified neurodevelopmental transcription factors (TFs) critical for GSC maintenance and tumorigenicity (Ikushima et al., 2009; Mehta et al., 2011; Rheinbay et al., 2013; Suvà et al., 2014). Cells co-expressing these TFs, along with stemness markers, are present in primary tumor specimens (Suvà et al., 2014). Furthermore, single-cell RNA sequencing (RNA-seq) analysis of primary GBMs identified tumor cells with transcriptional circuits reminiscent of in vitro GSC models (Patel et al., 2014).

Despite their analogous neurodevelopmental states, *in vivo* stem-like cells differ markedly in their expression of cell-cycle genes (Patel et al., 2014). In contrast to proliferative in vitro

间期
间期又分为三期。即DNA合成前期(G1期)、DNA合成期(S期)与DNA合成后期(G2期)。
1. G1期 (first gap) 从有丝分裂到DNA复制前的一段时间, 又称合成前期, 此期主要合成RNA和核糖体。该期特点是物质代谢活跃, 迅速合成RNA和蛋白质, 细胞体积显著增大。这一期的主要意义在于为下阶段S期的DNA复制作好物质和能量的准备。
2. S期 (synthesis) 即DNA合成期, 在此期, 除了合成DNA外, 同时还要合成组蛋白。DNA复制所需要的酶都在这一时期合成。
3. G2期 (second gap) 期为DNA合成后期, 是有丝分裂的准备期。在这一时期, DNA合成终止, 大量合成RNA及蛋白质, 包括微管蛋白和促成因子等。
分裂期
细胞分裂期 (mitosis) 需经前、中、后、末期, 是一个连续变化过程, 由一个母细胞分裂成为两个子细胞。一般需1~2小时。
1. 前期 (prophase) 染色体高度螺旋化, 逐渐形成染色体 (chromosome)。染色体短而粗, 强嗜碱性。两个中心体向相反方向移动, 在细胞中形成两极; 而后以中心粒为起始点开始合成微管, 形成纺锤体。随着核仁相染色体的螺旋化, 核仁逐渐消失。核被膜开始瓦解为离散的囊泡状内质网。
2. 中期 (metaphase) 细胞变为球形, 核仁与核被膜已完全消失。染色体均移到细胞的赤道平面, 从纺锤体两极发出的微管附着于每一个染色体的着丝点上。从中期细胞可分离得到完整的染色体群, 共46个, 其中44个为常染色体, 2个为性染色体。男性的染色体组型为44+XY, 女性为44+XX。分离的染色体呈短粗棒状或发夹状, 均由两个染色单体借狭窄的着丝点连接构成。
3. 后期 (anaphase) 由于纺锤体微管的活动, 着丝点纵裂, 每一染色体的两个染色单体分开, 并向相反方向移动, 接近各自的中心体。染色单体遂分为两组。与此同时, 细胞被拉长, 并由于赤道部细胞膜下方环行微丝束的活动, 该部缩窄, 细胞遂呈哑铃形。
4. 末期 (telophase) 染色单体逐渐解螺旋, 重新出现染色质丝与核仁; 内质网囊泡组合为核被膜; 细胞赤道部缩窄加深, 最后完全分裂为两个2倍体的子细胞。

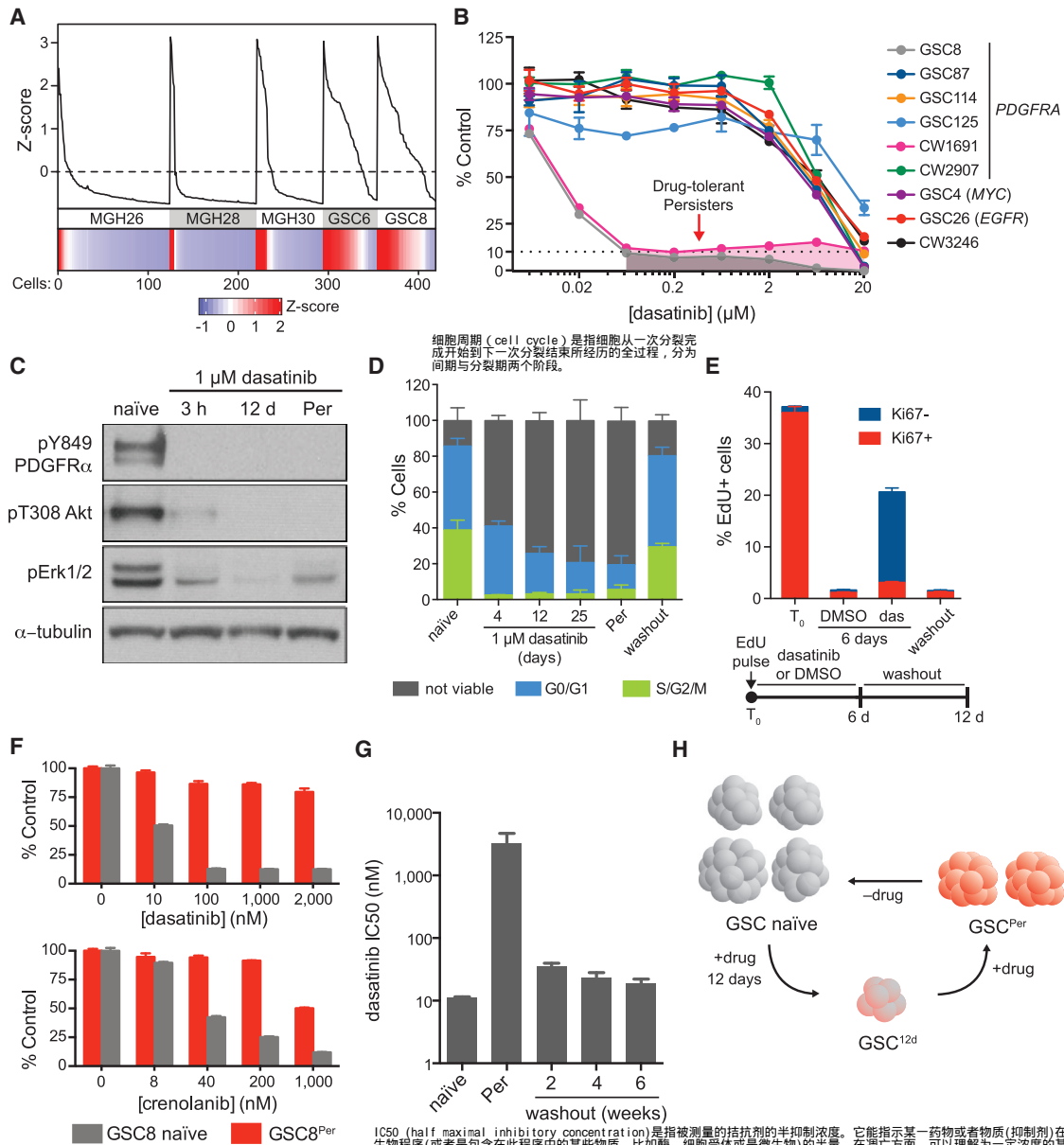


Figure 1. RTK Inhibition Prompts Emergence of Slow-Cycling Drug-Tolerant Persisters

(A) Line graph shows cell-cycle meta-signature Z scores (y axis) for ordered individual cells (x axis) for three primary tumors (MGH26, MGH28, and MGH30) and two GSC lines (GSC6 and GSC8). Lower panel: heatmap of cell-cycle meta-signature Z scores. More cells in GSC lines display increased cell-cycle expression in comparison to primary tumor specimens.

(B) Dose-response curves for treatment. Models were treated for 4 days with the exception of CW1691 (6 days). *PDGFRA*-amplified GSC8 and CW1691 display selective sensitivity (IC_{50} of ~ 10 nM) in comparison to other lines tested. Error bars represent SEM across three replicates. One of two biological replicates is shown.

(C) Immunoblots show levels of phosphorylated *PDGFR α* , Akt, and Erk1/2 upon dasatinib treatment for 3 hr (3 h), 12 days (12 d), and >8 weeks (Per) in GSC8. Dasatinib treatment significantly reduced levels of phosphorylated proteins. One of two biological replicates is shown.

(D) Stacked barplot shows the fraction of cells viable in G0/G1 and in S/G2/M (y axis) for GSC8 treated with dasatinib (1 μ M) at various time points (x axis). Washout refers to removal of dasatinib for >8 weeks. Error bars represent SD across at least three biological replicates.

(E) Stacked barplot summarizes flow cytometry data for Ki67 and EdU incorporation after EdU pulse (2 hr) and subsequent treatments. Dasatinib-treated cells maintained higher relative levels of EdU⁺ cells, which lose Ki67 positivity, compared to vehicle-treated cells. Further 6-day washout of dasatinib depletes EdU⁺ cells. Error bars represent SD across three biological replicates.

(F) Barplots show the relative percentage of cells (y axis) after 4-day drug treatments at various doses (x axis) in comparison to DMSO controls. GSC8^{Per} tolerates higher concentrations of *PDGFR* inhibitors (dasatinib and crenolanib) in comparison to GSC8 naive. Error bars represent SEM across six replicates. One of two biological replicates is shown.

(legend continued on next page)

models, tumor cells have relatively low expression of cell-cycle genes. This suggests that GSCs may adopt slow-cycling or quiescent states in vivo, consistent with the notion that cancer stem cells owe their refractory character to stable or transient quiescence (Sosa et al., 2014). Prior studies demonstrated that slow-cycling cells with stem-like properties promote tumor propagation and drug resistance in various cancer models (Chen et al., 2012; Roesch et al., 2010; Vanner et al., 2014).

We provide evidence that GSCs can adopt, and transition between, proliferative and slow-cycling states. We used the phenotype of reversible drug tolerance in RTK-dependent GSC lines to model the dynamic interconversion between these states. RTK inhibition led to rapid emergence of slow-cycling cells insensitive to RTK inhibitors and depleted for cell-cycle gene expression programs. These persister cells (GSC^{Per}) express increased levels of stemness markers and TFs and develop dependence on Notch signaling. Transition to the persister state is accompanied by histone demethylase (KDM) upregulation and widespread redistribution of histone H3 lysine 27 trimethylation (H3K27me3). The H3K27 demethylases KDM6A/B are essential for the slow-cycling state but are largely dispensable for the proliferative state. Our study highlights key roles for chromatin reorganization and developmental plasticity in GBM biology and suggests strategies for supplementing anti-proliferative therapies with modulators of epigenetic and developmental pathways.

RESULTS

Sustained Inhibition of Kinase Signaling Enriches for Slow-Cycling GSCs

GSCs maintained in serum-free neurosphere culture conditions share features with neural stem cells (NSCs) and effectively initiate tumors in xenotransplantation assays (Lathia et al., 2015). To investigate proliferative programs in GSCs, we compared single-cell transcriptomes of primary GBM cells to in vitro GSCs (Patel et al., 2014). In primary tumors, only a small fraction of cells displays proliferative markers (2%–20% Ki67⁺) (Louis et al., 2016) or expresses cell-cycle signatures (Patel et al., 2014). When we compared developmental and cell-cycle signatures, we found only a fraction of stem-like GBM tumor cells display proliferative signatures. In contrast, such signatures are evident in most in vitro GSCs (Figure 1A). While different GSC lines exhibit variable proliferation (Figure S1A) (Wakimoto et al., 2009), this potentially represents a critical distinction between in vitro and in vivo models.

We therefore considered whether proliferative in vitro GSCs could be induced to a non-proliferative state. We treated a panel of GSC lines with small molecule inhibitors of oncogenic signaling pathways (Figures 1B and S1B; Table S1). GSC8 and CW1691, both of which harbor focal amplification of *PDGFRA*, are highly sensitive to dasatinib (half maximal inhibitory concentration [IC₅₀] of ~10 nM) (Figure 1B), a platelet-derived growth

factor receptor (PDGFR)/Src inhibitor. By contrast, four other models derived from *PDGFRA*-amplified tumors—GSC87, GSC114, GSC125, and CW2907—are largely insensitive to dasatinib.

In agreement with PDGFR α being the relevant target of dasatinib in the sensitive models, GSC8 and CW1691 are also sensitive to crenolanib, a PDGFR inhibitor that does not appreciably inhibit Src (Figure S1C). Furthermore, overexpression of a drug-resistant PDGFR α mutant (D842V) (Dewaele et al., 2008) partially rescues GSC proliferation in the presence of dasatinib or imatinib, another PDGFR inhibitor (Figures S1D and S1E), while short hairpin RNA (shRNA) knockdown of PDGFR α decreased GSC proliferation (Figure S1F). Dasatinib treatment reduced phosphorylation of PDGFR α (pY849), Akt (pT308), and Erk1/2 (pT202/pY204, pT185/pY187) (Figures 1C and S1G). While off-target effects of dasatinib cannot be ruled out, these findings support RTK inhibition as the predominant effector of drug treatment in these models. GSC8 is also sensitive to the mitogen-activated protein kinase kinase (MEK) inhibitor PD0325901 (Figure S1B), suggesting that the effects of PDGFR α inhibition may operate via mitogen-activated protein kinase (MAPK) signaling.

Despite the effects of dasatinib, sustained exposure consistently yielded a persistent subpopulation that tolerates higher drug concentrations (Figure 1B). Specifically, treatment of naive GSC8 (1 μ M dasatinib, ~100 times IC₅₀) leads to an acute drop in the fraction of cycling, viable cells followed by a slow recovery (Figures 1D and S2A–S2D). 5-Ethynyl-2-deoxyuridine (EdU) pulse labeling followed by 6-day dasatinib treatment confirmed that initially cycling cells (EdU⁺) retained the label and transitioned to a Ki67[−] state (Figures 1E and S2E). Subsequent washout of dasatinib resulted in rapid loss of EdU⁺ cells. These data suggest that although many cells acutely die upon exposure to dasatinib, a subset of proliferative cells undergoes cell-cycle arrest but remains viable and slowly expands despite the presence of the drug. We refer to these drug-persistent cells as GSC8^{Per}. GSC8^{Per} lines could also be derived with inhibitors of downstream kinases, including MEK and CDK4/6 (Figures S1B, S1H, and S2F). We also derived persisters from an epidermal growth factor receptor (EGFR)-dependent line, GSC26, that tolerate higher concentrations of EGFR inhibitors (Figure S1I).

We isolated populations of GSC8^{Per} cultured in dasatinib for at least 8 weeks. These cells are relatively insensitive to dasatinib and crenolanib (Figure 1F) and still lack PDGFR α pY849 (Figure 1C), suggesting no mutation of PDGFR α -conferring resistance. We considered whether other genetic mechanisms might underlie drug tolerance in GSC8 persisters. It has been reported that drug tolerance to EGFR inhibitors may be mediated by reduction of *EGFR*⁺ extrachromosomal DNA and EGFR expression levels (Nathanson et al., 2014). In GSC8^{Per}, however, total levels of PDGFR α remained relatively constant or increased (Figures S1G and S1J), and low-coverage whole-genome

(G) Barplot shows dasatinib IC₅₀ values (y axis) for GSC8 naive, for GSC8^{Per}, and at different time points following dasatinib removal. Washout of dasatinib from GSC8^{Per} leads to resensitization to dasatinib-mediated growth arrest. Error bars represent SD of three biological replicates from separately derived GSC8^{Per} lines.

(H) Schematic illustrating formation of slow-cycling, drug-tolerant persisters. See also Table S1 and Figures S1 and S2.

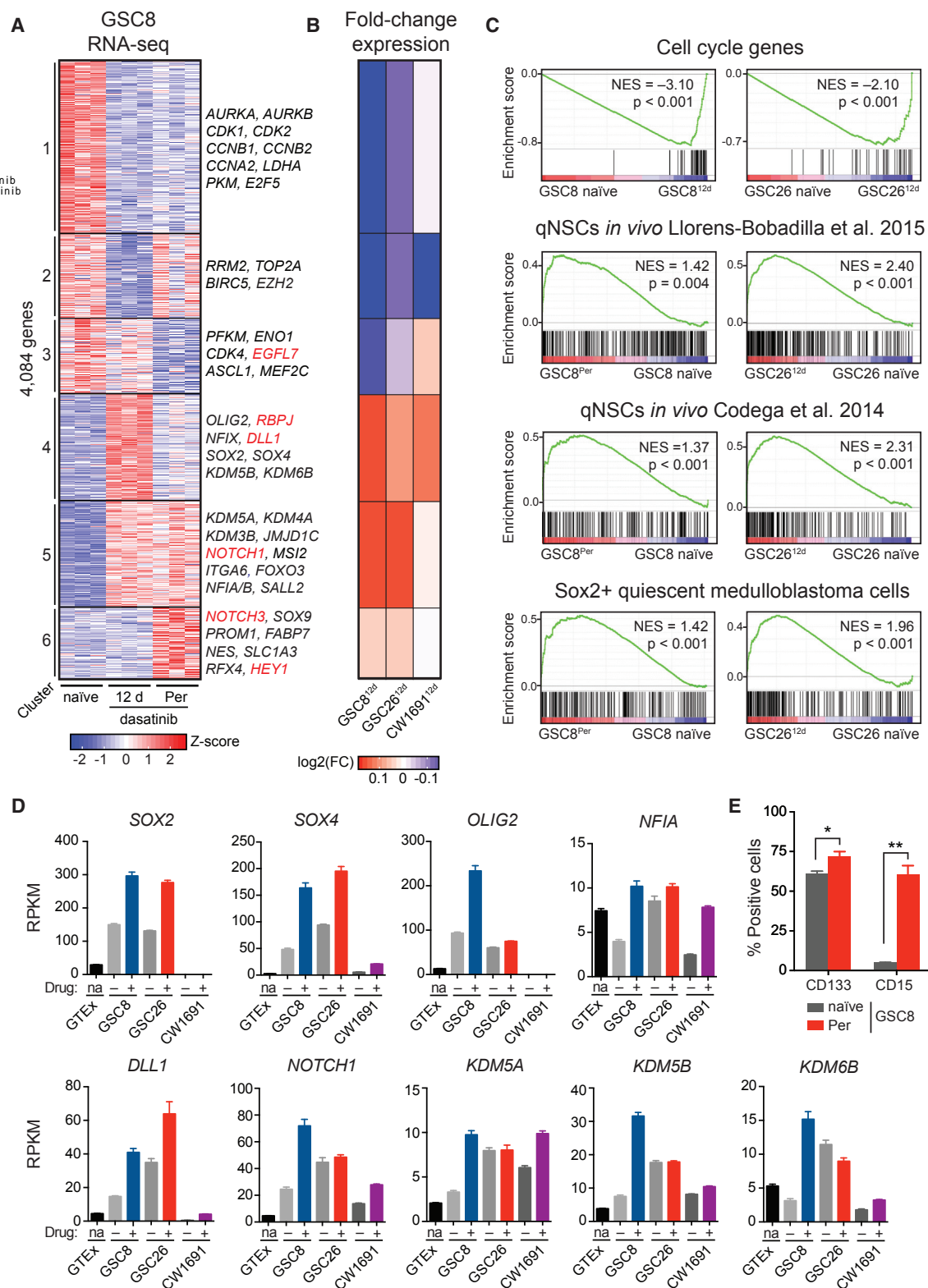


Figure 2. Transcriptional Programs Related to Slow Proliferation and Stemness Are Enriched in GSC8 Persisters

(A) Heatmap shows expression profiles of the 4,084 most variably expressed genes across GSC8 naïve, GSC8^{12d}, and GSC8^{Per}. K-means clustering was performed to distinguish sets of genes with coherent patterns of expression across the time course of dasatinib treatment. Data were generated from three biological replicates of separately derived GSC8^{12d} and GSC8^{Per} cultures. Color represents Z scores of gene expression across rows.

(legend continued on next page)

sequencing revealed no significant copy number changes at *PDGFRA* or other loci (Figure S1K). Most critically, the GSC8^{Per} state is reversible. Withdrawal of dasatinib permits full recovery of growth (Figure 1D), as well as re-sensitization to acute drug-induced arrest even after >4 months of chronic dasatinib treatment (Figure 1G). The rapidity and reversibility of acquired resistance support an epigenetic rather than a genetic tolerance mechanism, as demonstrated in several cancer cell lines (Easwaran et al., 2014; Knoechel et al., 2014; Koppikar et al., 2012; Sharma et al., 2010).

Persister GSCs Express Primitive Neurodevelopmental and Quiescence Signatures

To investigate the regulatory circuits that sustain persister GSCs, we profiled gene expression in GSC8^{Per}, in naive GSCs, and in short-term treated GSCs (GSC8^{12d}) at maximal arrest (Figure 1H). Clustering of the 4,084 genes with highest variability across these states revealed gene sets with coherent expression changes (Figure 2A; Table S2). Genes depleted in GSC8^{12d} (clusters 1–3) and GSC8^{Per} (clusters 1 and 3) were related to cell cycle and proliferation, consistent with reduced proliferation (Figures 2A, 2C, and S3A). By contrast, genes upregulated in GSC persisters (clusters 4–6) were enriched for signatures derived from quiescent NSCs (qNSCs) (Codega et al., 2014; Llorens-Bobadilla et al., 2015; Martynoga et al., 2013) and quiescent, stem-like medulloblastoma cells (Figures 2C and S3B) (Vanner et al., 2014). Profiling of GSC26 and CW1691 treated with gefitinib and dasatinib, respectively, revealed similar changes in expression for the respective GSC8-derived gene clusters (Figure 2B) and enrichment of quiescent gene signatures (Figures 2C and S3C).

Gene sets upregulated in persisters contain stemness factors previously linked to GSCs (Gangemi et al., 2009; Ikushima et al., 2009; Mehta et al., 2011; Suvà et al., 2014), as well as regulators implicated in stem-like tumor cells in vivo (Patel et al., 2014) (Figure 2A, clusters 4–6, and Figures 2D and S3D). GSC8^{Per} also upregulate classical stemness markers, such as PROM1 (CD133) and SSEA-1 (CD15) (Singh et al., 2004; Son et al., 2009) (Figures 2A, 2E, and S3E). Many of these TFs and markers are already expressed in naive GSCs but are upregulated on drug treatment (Figures 2D, 2E, and S3D). The persisters also upregulate multiple KDMs (Figures 2A, 2D, and S3F–S3I), including KDM3, KDM5, and KDM6 family members, some of which have been previously implicated in slow-cycling drug-resistant cell lines (Roesch et al., 2013; Sharma et al., 2010) and single-cell studies of primary GBM (Patel et al., 2014). Altogether, these expression changes are consistent with the notion

that GSC persisters transition to a slow-cycling state and upregulate transcriptional programs shared with qNSCs.

Notch Signaling Underlies GSC^{Per} Switch

The strong upregulation of prominent Notch signaling genes prompted us to investigate this pathway (Figures 2A and 2D). Various notch pathway genes were upregulated in GSC8^{Per}, including Notch ligands, receptors, and canonical downstream targets (Figures 3A, S4A, and S4B). Consistent with these changes, GSC8 persisters have high levels of Notch1 intracellular domain (N1ICD) (Figure 3B), the proteolytic cleavage product of activated Notch1 receptor that mediates gene induction. The dasatinib-insensitive *PDGFRA*-amplified models, GSC87 and CW2907, already express Notch pathway genes at higher levels, suggesting that they preexist in a Notch-high state (Figure 3C).

In considering whether Notch signaling is required for the slow-cycling state, we used a small molecule inhibitor of γ -secretase, a protease necessary for Notch activation (Kovall and Blacklow, 2010). Treatment with γ -secretase inhibitor (compound E) reduced GSC8^{Per} growth but had little effect on naive GSC8 (Figure 3D). Notch signaling can also be suppressed genetically using a dominant-negative form of mastermind-like (MAML) proteins (dnMAML), critical co-factors for Notch-mediated gene activation (Kovall and Blacklow, 2010; Maillard et al., 2004). Overexpression of dnMAML markedly reduced GSC8^{Per} proliferation but had little effect on naive GSC8 (Figure 3E). Conversely, overexpression of N1ICD was sufficient to induce a reversible growth reduction in GSC8 naive (Figures 3F and S4D–S4F). These data suggest that Notch activation allows GSCs to transition to a slow-cycling, RTK-independent state.

Primary GBM Tumors Contain Notch-Positive Cells Depleted for Proliferation Markers

To address the in vivo relevance of our findings, we co-stained primary GBM specimens from *PDGFRA*- and *EGFR*-amplified tumors for the Notch marker N1ICD and the proliferation marker Ki67. A subset of N1ICD⁺ cells is evident in variable proportions (4.2%–11.5%) in all specimens examined. Most N1ICD⁺ cells (90%–100%) were not Ki67⁺ (Figure 4A), suggesting that tumor cells with active Notch signaling are slow cycling.

We also integrated expression signatures from our in vitro GSC study with single-cell RNA-seq data for primary GBM tumors. We acquired RNA-seq profiles for 300 individual cells from one *EGFR*-amplified tumor (MGH66) and integrated published single-cell data from two additional *EGFR*-amplified tumors (Patel et al., 2014). We considered the following five

(B) Heatmap shows average changes in gene expression of clusters 1–6 in GSC8, GSC26, and CW1691 after 12-day treatment with gefitinib or dasatinib, respectively, compared to corresponding untreated control. Similar trends of gene expression change are evident in GSC8, GSC26, and CW1691 persisters. Color represents log₂ (fold change) gene expression, where the scale ranges from the minimum to the maximum value observed in GSC26^{12d} or CW1691^{12d}. (C) Gene set enrichment analysis (GSEA) shows enrichment of a cell-cycle meta-signature (upper panel), gene sets related to qNSCs (middle panels), and Sox2⁺ medulloblastoma cells (lower panel) across naive and persister states for GSC8 and GSC26. The cell-cycle gene signature is negatively enriched, while the quiescence gene signatures are positively enriched upon drug treatment. (D) Barplots show the expression levels (reads per kilobase per million mapped reads [RPKM], y axis) of *SOX2*, *SOX4*, *OLIG2*, *NFIA*, *DLL1*, *NOTCH1*, *KDM5A*, *KDM5B*, and *KDM6B* in normal human brain (GTEx), GSC8 naive, GSC8^{12d}, GSC26 naive, GSC26^{12d}, CW1691 naive, and CW1691^{12d}. Most genes are upregulated in drug-treated cells. Error bars represent SEM. (E) Barplot shows the fraction of cells (y axis) CD133⁺ or CD15⁺ by flow cytometry. GSC8^{Per} displays significantly increased positivity for CD133 and CD15 in comparison to GSC8 naive (Student's t test; *p < 0.05; **p < 0.01). Error bars represent SEM across three biological replicates. See also Tables S2–S4 and Figure S3.

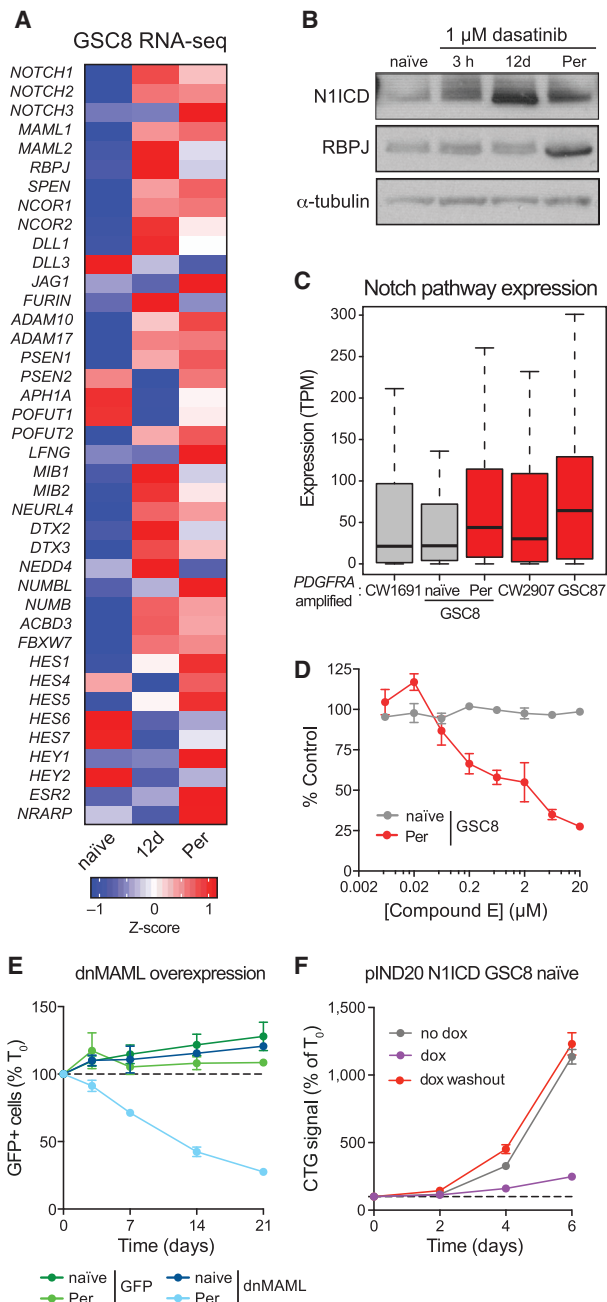


Figure 3. Notch Signaling Is Activated in GSC8^{Per}

(A) Heatmap shows the average expression of genes implicated in Notch signaling (Kopan and Ilagan, 2009) for GSC8 naive, GSC8^{12d}, and GSC8^{Per}. Gene expression was averaged over replicates within each condition; color represents Z scores.

(B) Immunoblots show levels of N1ICD and RBPJ in GSC8 naive and GSC8 treated with dasatinib for 3 hr (3h), 12 days (12d), and >8 weeks (Per). One of two biological replicates is shown.

(C) Boxplots show Notch pathway gene expression (transcripts per million [TPM], y axis) in different PDGFRA-amplified GBM lines. Notch signaling is increased in GSC8^{Per} and is significantly higher in insensitive cell lines compared to sensitive cell lines ($p < 10^{-7}$; Friedman test). Color indicates relative sensitivity (gray) or insensitivity (red) to dasatinib.

(D) Dose-response curves for 12-day compound E treatment are shown. GSC8^{Per} are preferentially sensitive in comparison to GSC8 naive. Error bars

represent SEM across four replicates. One of three biological replicates is shown.

gene signatures: (1) a naive GSC signature comprising genes in clusters 1–3 (Figure 2A), (2) a persister GSC signature comprising genes in clusters 4–6 (Figure 2A), (3) a cell-cycle signature, (4) a Notch-target gene signature derived by mapping N1ICD binding sites (see below), and (5) an in vivo qNSC signature (Codega et al., 2014).

We scored each tumor cell for each of these five signatures. Signatures for naive GSCs and cell cycle were commonly expressed in a small subset of tumor cells (Figure 4B), consistent with relatively low Ki67 positivity. Signatures for N1ICD-target genes and in vivo qNSCs scored in a distinct subset of persister-like tumor cells (Figures 4B and 4C). Altogether, these data indicate that primary GBMs contain a subset of cells that share features with persister GSCs, including Notch positivity, stem-like gene expression, and depletion of proliferation markers.

Notch Activity Targets Developmental Enhancers

To investigate how Notch signaling sustains persister GSCs, we mapped N1ICD and its co-factor recombining binding protein suppressor of hairless (RBPJ) by chromatin immunoprecipitation sequencing (ChIP-seq) across the three GSC8 states. Consistent with increased levels of N1ICD and RBPJ, we detected an ~6-fold increase in the number of N1ICD binding sites in GSC8^{12d} and GSC8^{Per}, relative to GSC8 naive (2,384 in GSC8^{Per} versus 370 in GSC8 naive), as well as increased signal intensities over these sites (Figures 5A and 5B). As expected, N1ICD binding sites largely overlapped RBPJ binding sites (1,750/2,384 in GSC8^{Per}), and the underlying DNA sequences are enriched for RBPJ recognition motifs (Figure 5C). Consistent with prior studies in lymphoid cells (Wang et al., 2011), N1ICD binds primarily to distal sequences containing the active enhancer mark H3K27ac (Figures 5D, 5E, and S5A) (ENCODE Project Consortium, 2012).

To identify putative Notch target genes, we assigned N1ICD peaks detected in GSC8 naive, GSC8^{12d}, or GSC8^{Per} to the nearest gene promoter. We focused on 1,696 target genes identified in GSC8^{12d} and/or GSC8^{Per}, but not in GSC8 naive (Table S3). Consistent with a primary role in transcriptional activation, these candidate N1ICD targets were predominantly upregulated in GSC8^{12d} and GSC8^{Per}, relative to GSC8 naive (Figures 5E and 5F), and enriched for Notch pathway and neurodevelopmental genes, as well as various canonical Notch targets (Figures 5D, S5B, and S5C). Illustrative examples are the HEY1 and HES5 loci (Figure 5D): HEY1 is associated with poor survival in GBM patients (Hulleman et al., 2009), and HES5 is implicated in

represent SEM across four replicates. One of three biological replicates is shown.

(E) Line graph shows the fraction of GFP⁺ cells normalized to day 0 (T_0) (y axis) over a time course following induced overexpression of dnMAML-GFP or GFP control. dnMAML overexpression selectively depleted GFP⁺ cells in GSC8^{Per}. Error bars represent SEM across three replicates. One of two biological replicates is shown.

(F) Line graphs show cell growth as relative CellTiter-Glo (CTG) values normalized to T_0 (y axis) over a time course (x axis) following doxycycline (dox)-induced N1ICD overexpression. N1ICD overexpression in GSC8 naive reduced proliferation but is reversed upon dox washout. Error bars represent SEM across three replicates. One of three biological replicates is shown. See also Figure S4.

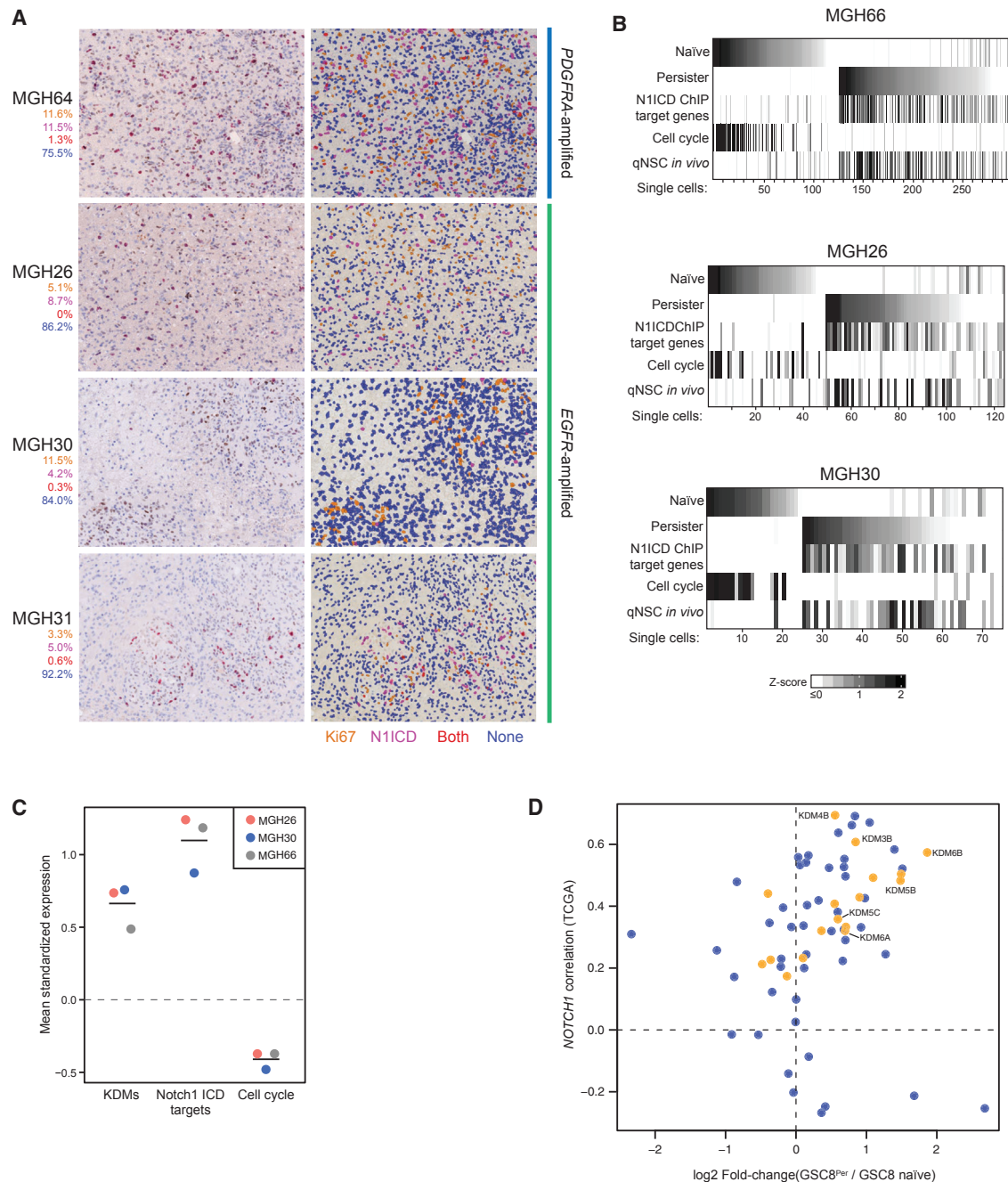


Figure 4. Slow-Cycling, Notch-High Cells Are Present in Primary GBM Tumors

(A) Images show hematoxylin staining and immunohistochemistry for N1ICD and Ki67 in patient primary GBM tumors, demonstrating that a subpopulation of N1ICD⁺ cells are slow cycling. Left panels: unenhanced images. Right panels: enhanced pseudocolored images. Percentages represent the fraction of total cells that are Ki67⁺ only (orange), N1ICD⁺ only (magenta), double positive (red), and double negative (blue).

(B) Heatmap shows mean expression of gene sets derived from GSC8 naive (Figure 2A, clusters 1–3) and GSC8^{Per} (Figure 2A, clusters 4–6), as well as N1ICD GSC8^{Per} target genes, a cell-cycle signature, and a qNSC *in vivo* signature (rows) across single tumor cells (columns) in three EGFR-amplified tumors (MGH66, MGH30, and MGH26). K-means clustering of columns identified groups of cells with similar expression profiles. Clusters were order based on expression of GSC8 naive or GSC8^{Per} signatures. Colors correspond to Z scores calculated across individual cells; in this representation, negative Z scores are mapped to 0.

(C) Dotplot shows mean expression (y axis) of KDM, Notch, and cell-cycle signature gene sets within persister-like cells (top quintile) in MGH26, MGH30, and MGH66 (x axis) (see B). Expression values were standardized (mean = 0; SD = 1)—observed deviations from zero reflect expression changes relative to all cells. Horizontal bars correspond to mean values for persister-like cells.

(D) For each annotated chromatin enzyme gene, scatterplot shows the correlation between its expression and NOTCH1 expression across all TCGA samples (y axis) versus its expression change in GSC8^{Per} relative to GSC8 naive (x axis). KDMs are highlighted in yellow.

See also Table S5.

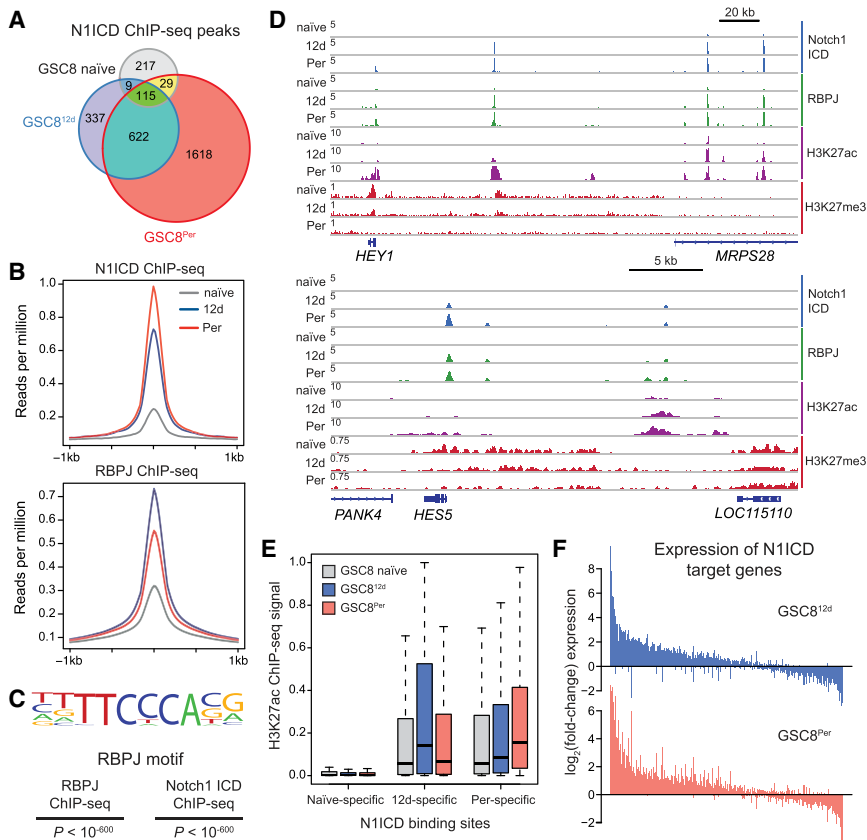


Figure 5. N1ICD Binds to Neurodevelopmental Enhancers in GSC Persisters

(A) Venn diagram shows the number and overlap of N1ICD ChIP-seq peaks across GSC8 naive, GSC8^{12d}, and GSC8^{Per} states. N1ICD localizes to fewer regions in GSC8 naive (368 peaks) and shows increased binding upon drug treatment (1,083 and 2,384 in GSC8^{12d} and GSC8^{Per}, respectively).

(B) ChIP-seq profile plots show the ChIP-seq signal (y axis, reads per million [rpm]) of N1ICD (upper panel) and RBPJ (lower panel) across peaks for each respective protein. The x axis shows flanking regions of ± 1 kb around the peak center.

(C) Consensus RBPJ motif logo detected in N1ICD and RBPJ ChIP-seq peaks in GSC8^{Per}. The corresponding p values are shown.

(D) ChIP-seq profiles show the ChIP-seq signal (y axis, rpm) of N1ICD, RBPJ, H3K27ac, and H3K27me3 at the *HEY1* (upper panel) and *HES5* (bottom panel) loci.

(E) Boxplots show H3K27ac levels of GSC8 naive, GSC8^{12d}, and GSC8^{Per} within 1.5 kb windows centered at NICD peaks identified within GSC8 naive (left), GSC8^{12d} (middle), and GSC8^{Per} (right). For each condition, H3K27ac levels were significantly higher within the corresponding condition-specific N1ICD peaks (GSC8^{12d}-specific NICD peaks: GSC8 naive versus GSC8^{12d}, $p < 10^{-15}$; GSC8^{Per}-specific NICD peaks: GSC8 naive versus GSC8^{Per}, $p < 10^{-16}$; Wilcoxon test).

(F) Barplots show log₂ (fold change) in gene expression of N1ICD target genes specifically identified in GSC8^{12d} or GSC8^{Per} for GSC8^{12d} (upper panel) and GSC8^{Per} (lower panel). Genes were sorted decreasingly according to the added fold change.

See also Figure S5.

qNSCs (Imayoshi et al., 2010). In addition to canonical targets, N1ICD bound H3K27ac-marked distal elements in the vicinity of many neurodevelopmental master regulators (e.g., SOX TFs and *OLIG1/2*) and several pro-survival genes (Figure S5D). These N1ICD and RBPJ binding patterns support a direct mechanistic role for Notch signaling in the activation of regulatory elements and neurodevelopmental genes in slow-cycling GSC persisters.

Dynamic Histone Acetylation and Demethylation Accompany GSC^{Per} Switch

The dynamic acetylation of N1ICD-bound elements prompted us to investigate global chromatin alterations associated with the persister transition. We mapped H3K27ac genome-wide in naive GSC8, GSC8^{12d}, and GSC8^{Per} and called enriched intervals, identifying an average of 12,938 sites in each GSC state (naive: 12,412; GSC8^{12d}: 12,940; GSC8^{Per}: 13,462). Approximately 63% of these sites are >5 kb from any annotated transcriptional start site, thus representing candidate distal regulatory elements or enhancers. These enhancer-like elements are dynamic in activity ($\sim 25\%$ common to all states and $\sim 50\%$ specific to one state).

We used K-means clustering to distinguish sets of promoter- and enhancer-like elements with related patterns of activity across the three GSC8 states (Figure 6A). We scanned the DNA sequences underlying the corresponding clusters for over-represented TF motifs (Figure 6A). The resulting predictions

of differential TF activity are largely concordant with the TF expression patterns derived by RNA-seq (Figure 2A). GSC8 naive-specific elements (Figure 6A, clusters II and III) are enriched for MEF2 motifs, consistent with high expression of MEF2C and its dimerization partner ASCL1 in the naive state (Figure 2A, cluster 3) (Black et al., 1996). ASCL1 has been previously implicated in proliferative stem cell populations (Rheinbay et al., 2013). GSC8^{12d}-specific elements (Figure 6A, clusters IV and V) are enriched for Foxo motifs, in agreement with upregulation of FOXO3 (Figure 2A, cluster 5, and Figure S3D), a TF with established roles in qNSCs (Paik et al., 2009; Renault et al., 2009). GSC8^{Per}-specific elements (Figure 6A, clusters VI and VII) are enriched for SOX and NF1 motifs, consistent with increased expression of these TFs in GSC8^{Per}. Thus, concordant differences in regulatory element activity and TF expression distinguish the respective GSC states and implicate neurodevelopmental regulatory programs in persister GSCs.

Many neurodevelopmental and Notch pathway genes are established targets of Polycomb repressors and the associated histone mark H3K27me3, which restrain their activity in non-expressing cell types (Simon and Kingston, 2013). The H3K27 methyltransferase EZH2 is downregulated in GSC persisters, while the H3K27 demethylases KDM6A and KDM6B are among a large set of KDMs that are upregulated (Figures 2A, S3G, and S3H). We therefore mapped and compared the distribution of H3K27me3 across naive GSC8, GSC8^{12d}, and GSC8^{Per}. Many

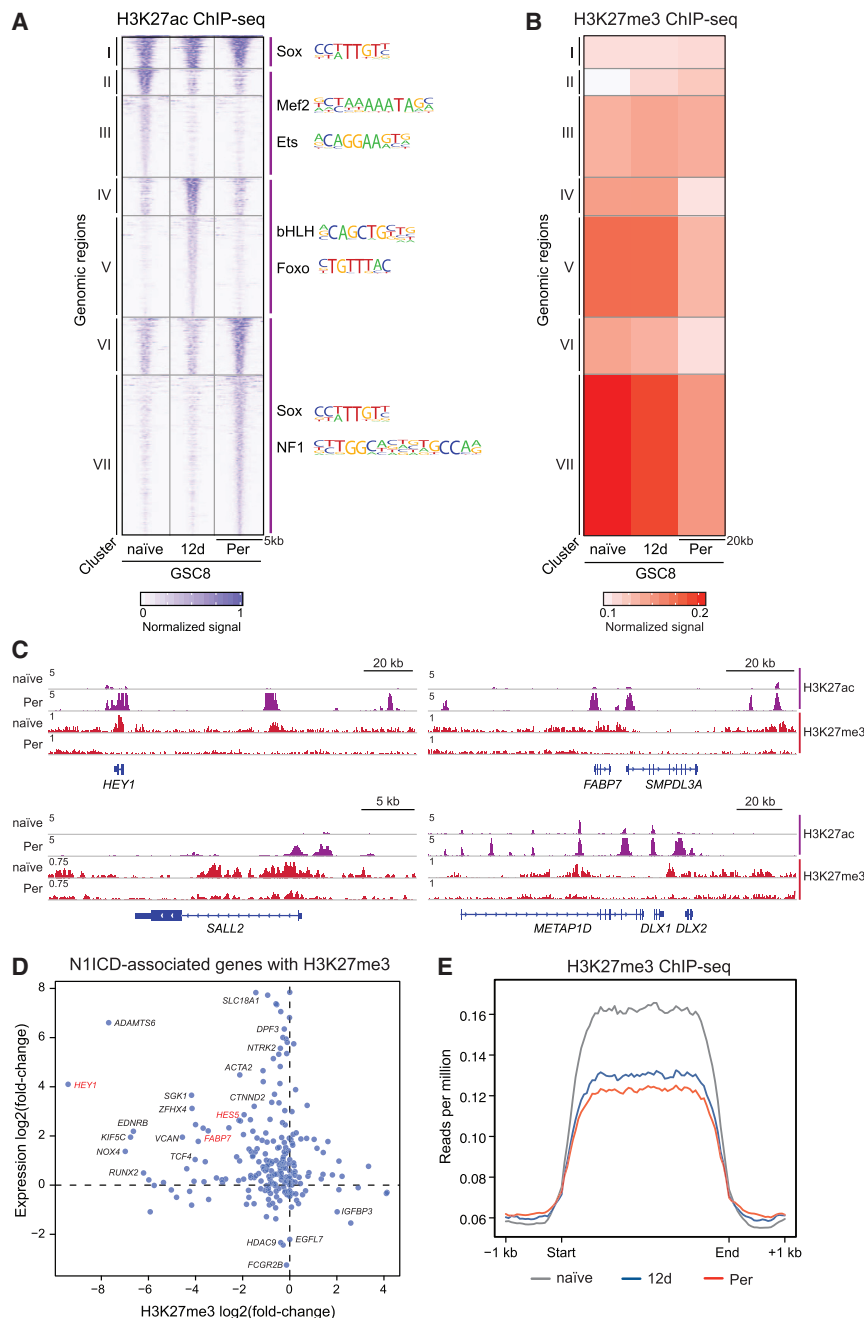


Figure 6. H3K27me3 Redistribution Accompanies Re-activation of Neurodevelopmental Genes

(A) Heatmap shows the normalized H3K27ac ChIP-seq signal for GSC8 naive, GSC8^{12d}, and GSC8^{Per} across different genomic intervals (rows). K-means clustering of rows identified groups of H3K27ac regions that are shared (I), naive enriched (II and III), GSC8^{12d} enriched (IV and V), and GSC8^{Per} enriched (VI and VII). Color corresponds to the normalized ChIP signal.

(B) Heatmap shows the average normalized ChIP-seq signal for H3K27me3 for groups of genomic intervals derived from clustering analysis in (A). H3K27me3 levels are depleted in cluster VI and VII. H3K27me3 signals were calculated within 20 kb windows centered on H3K27ac peaks, respectively. Color corresponds to normalized ChIP signal.

(C) ChIP-seq profiles show the ChIP-seq signal (y axis, reads per million [rpm]) for H3K27ac and H3K27me3 at genomic loci of *HEY1*, *FABP7*, *DLX2*, and *SALL2*.

(D) Scatterplot shows changes in expression (y axis) and intragenic H3K27me3 levels (x axis) of genes associated with an N1ICD peak in GSC8^{Per} that contain at least one H3K27me3 peak in GSC8 naive, GSC8^{12d}, or GSC8^{Per}. The y axis represents log2 (fold change) in gene expression comparing GSC8^{Per} to GSC8 naive. The x axis represents log2 (fold change) of intragenic H3K27me3 levels comparing GSC8^{Per} to GSC8 naive.

(E) ChIP-seq profile plots show the H3K27me3 ChIP-seq signal (y axis, rpm) across all H3K27me3 domains (>10 kb) in GSC8 naive (gray), GSC8^{12d} (blue), and GSC8^{Per} (red). The x axis represents size-scaled H3K27me3 domains, with ± 1 kb flanking regions.

See also Figure S6.

N1ICD-associated loci marked by H3K27me3 in naive GSC8 undergo coincident H3K27 demethylation, upregulation, and H3K27 acetylation upon transition to the persister state (Figures 6D and S5E). Examples include the *HEY1* and *HES5* loci, where increased binding of N1ICD and RBPJ is accompanied by gain of H3K27ac and loss of H3K27me3 (Figure 5D).

Broadly, we considered whether increased H3K27ac at enhancer-like elements in GSC8^{Per} is associated with a reduction in H3K27me3. Many of these elements are initially marked by H3K27me3 but are strongly depleted for this repressive mark upon activation in GSC8^{12d} and/or GSC8^{Per} cells (Figures 6A–6C, cluster VII). Consistent with established roles for the

H3K27ac elements tend to have diminished H3K27me3 in GSC8^{Per} (Figures 6A and 6B, clusters II and III). This suggests that the transition from naive to persister state is accompanied by a global loss of H3K27me3 from *cis*-regulatory elements. To gain more systematic insight, we called H3K27me3-enriched intervals genome-wide in each of the three GSC cell states. H3K27me3 levels across these intervals are markedly reduced in GSC8^{12d} and GSC8^{Per}, relative to naive (Figure 6E). A reduction in H3K27me3 levels also occurred following treatment of GSC8 naive cells with MEK inhibitor PD0325901 (Figure S6A) and, to a lesser extent, following treatment of GSC26 cells with an EGFR inhibitor (Figure S6B). Altogether, these data suggest

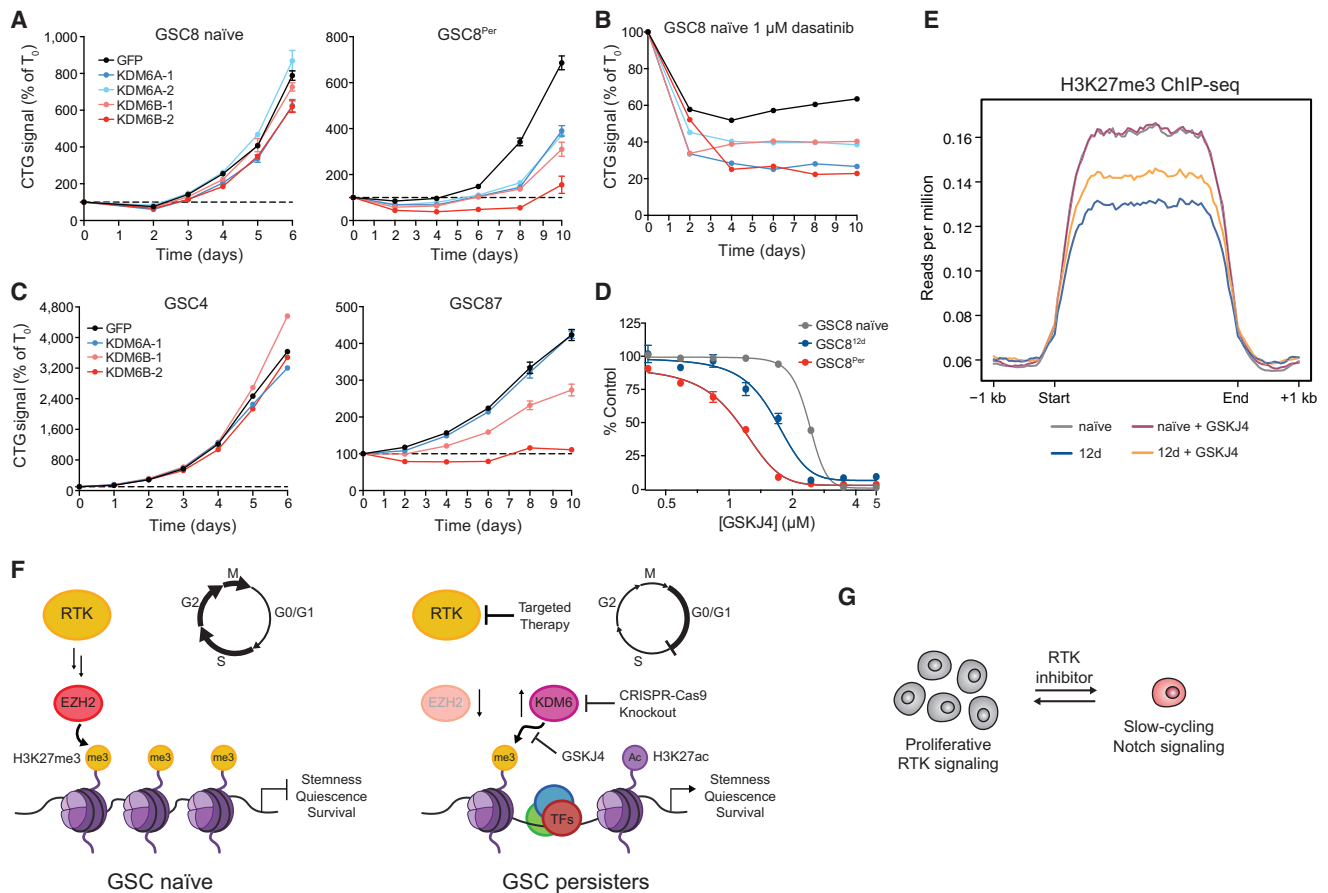


Figure 7. KDM6 Is Essential in GSC Persisters

(A–C) Line graphs show cell growth as relative CellTiter-Glo (CTG) values normalized to T_0 (y axis) over a time course (x axis) following CRISPR-Cas9-mediated knockout of respective genes. Knockout of KDM6A and KDM6B modestly affected the proliferation of GSC8 naive (A, left panel) but significantly impaired proliferation of GSC8^{Per} (A, right panel) and emergence of persisters (B). Knockout of KDM6B preferentially affected the proliferation of GSC87 (C, right panel), which displays persister-like characteristics. Error bars represent SEM across at least three replicates. One of two biological replicates is shown.

(D) Dose-response curves for 4-day GSKJ4 treatment are shown. GSC8^{12d} and GSC8^{Per} are preferentially sensitive to GSKJ4 in comparison to GSC8 naive. Error bars represent SEM across three replicates. One of three biological replicates is shown.

(E) ChIP-seq profile plots show the H3K27me3 ChIP-seq signal (y axis, rpm) across all H3K27me3 domains (>10 kb) in GSC8 naive (gray), GSC8^{12d} (blue), GSC8 treated with GSKJ4 (8 days, 1.5 μ M, purple), and GSC8^{12d} treated with GSKJ4 (8 days, 1.5 μ M, orange) starting after 4 days of initial dasatinib treatment. The x axis represents size-scaled H3K27me3 domains, with ± 1 kb flanking regions.

(F) Schematic illustrating a proposed model, whereby EZH2 loss and KDM6B upregulation may facilitate H3K27 remodeling and subsequent activation of stemness programs.

(G) Cartoon depicting the switch between RTK- and Notch-dependent states that may parallel antagonism between these pathways in normal neurodevelopment.

See also Table S4 and Figures S6 and S7.

that the activation of neurodevelopmental loci and Notch pathway genes is accompanied by pervasive acetylation of *cis*-regulatory elements and may be facilitated by a global redistribution of H3K27me3-repressive chromatin.

H3K27me3 Demethylases KDM6A/B Are Essential for GSC Persisters

Multiple KDMs are coordinately upregulated in the persisters (Figure 2A), while Notch-high tumors and Notch-high tumor compartments also exhibit significantly higher KDM expression (Brennan et al., 2013; Patel et al., 2014; Verhaak et al., 2010) (Figures 4C and 4D). Moreover, widespread redistribution of H3K27me3 in cells exiting the cell cycle is suggestive of active

histone demethylation. Altogether, these data implicate the H3K27 demethylases KDM6A/B in the transition or maintenance of persister GSCs. We therefore separately knocked out *KDM6A* and *KDM6B* in GSC8 naive and GSC8^{Per} using clustered regularly interspaced short palindromic repeats-CRISPR associated protein 9 (CRISPR-Cas9) genome editing (Doench et al., 2014) and single-guide RNAs (sgRNAs) targeting their catalytic domains (Shi et al., 2015) (Figure S7A).

KDM6A and *KDM6B* knockout minimally affected GSC8 naive cell growth (Figure 7A, left panel). By contrast, GSC8^{Per} cells were highly sensitive to knockout of either demethylase (Figure 7A, right panel); growth reduction afforded by *KDM6B* knockout was most pronounced, consistent with a reported

pro-oncogenic role for KDM6B (Hashizume et al., 2014; Ntziachristos et al., 2014). Moreover, GSC8 naive cells lacking *KDM6A* or *KDM6B* were less effective at forming persisters upon dasatinib treatment (Figure 7B).

To further explore this KDM6 dependency, we expanded our studies to other GSC models: GSC4 and GSC87. GSC4 is *MYC* amplified, is rapidly proliferating, and expresses a cell-cycle gene signature akin to naive GSC8 cells, while GSC87 is slow-cycling and expresses a persister-like gene signature at baseline (Figure S7B). GSC87 is highly CD133⁺, Notch dependent, and insensitive to dasatinib despite focal *PDGFRA* amplification, and it displays H3K27ac profiles similar to those of GSC8^{Per} (Figures 1B, S4C, and S7B–S7D). Knockout of either *KDM6A* or *KDM6B* had negligible effects on GSC4, but *KDM6B* knockout significantly impaired persister-like GSC87 (Figure 7C). These data support general roles for KDM6 demethylases in the transition and maintenance of slow-cycling, persister-like GSCs.

To evaluate the contributions of KDM6 enzymatic activity, we treated GSCs with the small molecule inhibitor GSKJ4 (Kruidenier et al., 2012) (Figures 7D and 7E). GSKJ4 treatment (1.5 μ M) had negligible effects on the preexisting H3K27me3 landscape of naive GSC8 but rescued the H3K27me3 loss seen upon dasatinib treatment (Figures 7E and S6C). GSKJ4 treatment did not significantly increase H3K4me3 in these models, supporting its selectivity for KDM6A/B at the doses used (Heinemann et al., 2014) (Figures S6D and S6E). These results support the notion that KDM6 contributes to the global H3K27me3 alterations in dasatinib-treated GSCs.

Consistent with our knockout data, GSKJ4 compromised proliferation of GSC8^{12d} and GSC8^{Per} at doses tolerated by naive GSC8 (Figure 7D). Likewise, GSC8 persisters derived from sustained MEK inhibition are preferentially sensitive to GSKJ4 (Figure S7E). By contrast, GSC persisters displayed no preferential sensitivity to GSKJ5, an inactive isomer of GSKJ4 (Kruidenier et al., 2012), or to KDM5-C70, a recently described KDM5-selective inhibitor (Johansson et al., 2016) (Figures S7E and S7F). Lastly, we found that GSC87, which exhibits persister-like features at baseline, showed increased sensitivity to GSKJ4, relative to the *PDGFRA*-dependent line CW1691 (Figure S7G). Thus, preferential KDM6 dependency may be a general characteristic of persister-like GSCs. Altogether, these data suggest that reconfiguration of H3K27me3 landscapes by histone demethylases facilitates the activation of regulatory elements and neurodevelopmental gene expression programs required for the drug-tolerant persister GSC state (Figure 7F).

DISCUSSION

Reversible transitions between epigenetic states enable tumor cells to adapt to different pressures, including conventional and targeted therapy (Easwaran et al., 2014; Knoechel et al., 2014; Koppikar et al., 2012; Roesch et al., 2013; Sharma et al., 2010). Such transitions could involve de novo states accessible only to malignant cells or may parallel aspects of normal developmental hierarchies. We show that patient-derived GSCs can evade RTK inhibition and other anti-proliferative therapies by regressing to a slow-cycling, Notch-dependent state (Figure 7G). We also establish that the GSC persister transition

is characterized by widespread remodeling of repressive chromatin and dependency on the H3K27 demethylases KDM6A/B.

An expanding body of literature supports a cancer stem cell model in GBM, wherein stem-like cells with differentiation potential mediate tumor propagation. GSCs are thought to resist current therapies and thus underlie inevitable relapse. Their refractory nature could relate in part to a subset of GSCs with a slow-cycling phenotype that is innately resistant to therapy (Chen et al., 2012; Lathia et al., 2015). Our analysis of clinical specimens by multi-spectral imaging and single-cell RNA-seq confirms that primary GBMs contain cells with persister-like features, including Notch positivity, high KDM expression, and low cell-cycle gene expression. These tumors were analyzed before therapy, which suggests that persister-like GSCs may preexist in GBMs. In agreement with this notion, one of our patient-derived models, GSC87, which is insensitive to PDGFR inhibitors despite harboring focal *PDGFRA* amplification, preexists in a persister-like state and is dependent on Notch signaling and KDM6. These findings provide a potential mechanistic explanation for innate drug resistance of GSCs and emphasize the need to identify therapeutic strategies to eliminate this refractory tumor compartment.

Several cancer cell line models of reversible drug resistance, including lung cancer lines tolerant to EGFR inhibitor (Sharma et al., 2010) and melanoma lines resistant to B-rapidly accelerated fibrosarcoma (BRAF) inhibitors (Roesch et al., 2013), upregulate and become dependent on KDM5 enzymes, which remove an activating mark, H3K4 methylation. By contrast, while GSC persisters upregulate several KDMs, they show a particular dependency on KDM6 enzymes, which remove the repressive mark, H3K27me3. Consistently, the transition to the persister state is accompanied by widespread redistribution of this repressive modification, with striking loss occurring at developmental loci undergoing activation. KDMs can also be induced by other stressors, including cell-cycle arrest (Agger et al., 2009; Ene et al., 2012), DNA damage (Williams et al., 2014), hypoxia (Black et al., 2015; Xia et al., 2009), and inflammation (De Santa et al., 2007). The ensuing demethylation may allow activation of alternative *cis*-regulatory elements and pathways to support survival and adaptation (Easwaran et al., 2014). Chromatin structure is widely implicated in cell fate restriction, and its disruption by KDM-mediated demethylation appears central to the emergence of persister GSCs. Whether KDM6 enzymes play general roles in drug tolerance, or facilitate re-activation of primitive developmental programs in GSC persisters, awaits further study.

We also establish a critical and specific role for Notch signaling in the persister GSCs. Notch signaling has been shown to activate neurodevelopmental programs in NSCs (Aguirre et al., 2010; Imayoshi and Kageyama, 2011; Mizutani et al., 2007). Notch activity in GSC^{Per} activates *cis*-regulatory elements that drive expression of master regulators of neurodevelopment and qNSCs. An important question remains about whether the epigenetic switch between RTK- and Notch-dependent GSC states emulates the antagonism between these signaling programs in NSCs, wherein Notch signaling is associated with quiescence and RTK signaling is associated with NSC activation. If so, proliferative heterogeneity within the tumor hierarchy may reflect aspects of a conserved developmental mechanism. A similar parallel was also suggested in low-grade glioma (Giachino et al., 2015), in which Notch signaling may promote a

less aggressive, slow-cycling population, suggestive of a tumor suppressor role. Yet in the context of drug treatment, this promotion of a slow-cycling state may have the untoward consequence of conferring resistance. The Notch dependency of the refractory GSC state may thus portend opportunities for combination therapy, some of which are now being explored in preclinical and early clinical studies (Cenciarelli et al., 2014; Xu et al., 2016; Yahyanejad et al., 2016).

In summary, we present a reversible epigenetic transition that enables GSCs to transition between proliferative and slow-cycling states, which may enable GBM tumors to propagate, adapt, and persist in the face of environmental and therapeutic pressures. Our work also reveals specific mechanisms by which developmental programs and epigenetic regulators facilitate this transition and sustain alternative states. A better understanding of these developmental programs and epigenetic mechanisms, and how they may be modulated, will be essential for developing effective therapeutic strategies that address malignant hierarchies and slow-cycling cancer cells in GBM and other tumors.

STAR★METHODS

Detailed methods are provided in the online version of this paper and include the following:

- **KEY RESOURCES TABLE**
- **CONTACT FOR REAGENT AND RESOURCE SHARING**
- **EXPERIMENTAL MODEL AND SUBJECT DETAILS**
 - GSC Derivation and Cell Culture
 - GSC Persisters
 - Primary Patient Specimens
- **METHOD DETAILS**
 - Cell Growth Assays
 - CRISPR-Cas9 and shRNA Experiments
 - Overexpression Studies
 - Flow Cytometric Analysis
 - Immunohistochemistry and Spectral Imaging of Primary GBM Specimens
 - Immunoblotting
 - Tumor Dissociation
 - Fluorescence-activated cell sorting of primary tumors
 - Single-cell whole transcriptome amplification, library construction, and sequencing
 - Real-Time Quantitative RT-PCR and RNA-seq Library Preparation
 - ChIP-seq
- **QUANTIFICATION AND STATISTICAL ANALYSIS**
 - Levels phosphorylated PDGFR α , Akt, and Erk1/2
 - Cell growth assays (Cell-titer Glo)
 - CRISPR-Cas9 and shRNA experiments
 - Overexpression studies
 - Flow Cytometric Analysis
 - Immunohistochemistry and Spectral Imaging of Primary GBM Specimens
 - Single-cell RNA-seq data analysis
 - Population RNA-seq analysis
 - ChIP-seq data analysis
 - ChIP-seq Binding Profiles
- **DATA AND SOFTWARE AVAILABILITY**

SUPPLEMENTAL INFORMATION

Supplemental Information includes seven figures, five tables and can be found with this article online at <http://dx.doi.org/10.1016/j.stem.2016.11.003>.

AUTHOR CONTRIBUTIONS

B.B.L., C.S., A.P.P., and B.E.B. designed the study and wrote the manuscript. B.B.L., A.P.P., L.K.D., S.M.G., T.E.M., A.S.V., C.H.H., C.D.C., S.J.R., S.J.S., and F.J.N. performed experimental work. C.S., B.B.L., and W.A.F. performed computational analyses. P.v.G., H.W., D.P.C., J.N.R., J.C.A., and M.L.S. provided reagents and conceptual advice.

ACKNOWLEDGMENTS

We thank S. Muller-Knapp and the Structural Genomics Consortium (Oxford, UK), Russell Ryan, Nicolò Riggi, and Henry Pelish for helpful discussions. We thank David Sabatini and Kris Wood for Notch1 intracellular domain-pcw107 and William Hahn and David Root for p-DONR223-PDGFR α M260I. B.B.L. is supported by a Jane Coffin Childs Memorial Fund postdoctoral fellowship. C.S. is supported by a European Molecular Biology Organization (EMBO) fellowship (ALTF 654-2014) and a Swiss National Science Foundation fellowship. P.v.G. is supported by an EMBO Fellowship (ALTF 1207-2014). A.P.P. is supported by the NIH/NINDS (R25NS065743). W.A.F. is supported by an American Brain Tumor Association grant. B.E.B. is an American Cancer Society research professor. This research was supported by funds from the Howard Hughes Medical Institute, the National Human Genome Research Institute, the National Cancer Institute (P50CA165962), and the National Brain Tumor Society.

Received: September 16, 2016

Revised: October 6, 2016

Accepted: October 31, 2016

Published: December 15, 2016

REFERENCES

- Agger, K., Cloos, P.A.C., Rudkjaer, L., Williams, K., Andersen, G., Christensen, J., and Helin, K. (2009). The H3K27me3 demethylase JMJD3 contributes to the activation of the INK4A-ARF locus in response to oncogene- and stress-induced senescence. *Genes Dev.* 23, 1171–1176.
- Aguirre, A., Rubio, M.E., and Gallo, V. (2010). Notch and EGFR pathway interaction regulates neural stem cell number and self-renewal. *Nature* 467, 323–327.
- Anders, S., and Huber, W. (2010). Differential expression analysis for sequence count data. *Genome Biol.* 11, R106.
- Bao, S., Wu, Q., McLendon, R.E., Hao, Y., Shi, Q., Hjelmeland, A.B., Dewhirst, M.W., Bigner, D.D., and Rich, J.N. (2006). Glioma stem cells promote radioresistance by preferential activation of the DNA damage response. *Nature* 444, 756–760.
- Black, B.L., Ligon, K.L., Zhang, Y., and Olson, E.N. (1996). Cooperative transcriptional activation by the neurogenic basic helix-loop-helix protein MASH1 and members of the myocyte enhancer factor-2 (MEF2) family. *J. Biol. Chem.* 271, 26659–26663.
- Black, J.C., Atabakhsh, E., Kim, J., Biette, K.M., Van Rechem, C., Ladd, B., Burrows, P.D., Donado, C., Mattoo, H., Kleinstiver, B.P., et al. (2015). Hypoxia drives transient site-specific copy gain and drug-resistant gene expression. *Genes Dev.* 29, 1018–1031.
- Brennan, C.W., Verhaak, R.G.W., McKenna, A., Campos, B., Nouthmeh, H., Salama, S.R., Zheng, S., Chakravarty, D., Sanborn, J.Z., Berman, S.H., et al.; TCGA Research Network (2013). The somatic genomic landscape of glioblastoma. *Cell* 155, 462–477.
- Cenciarelli, C., Marei, H.E.S., Zonfrillo, M., Pierimarchi, P., Paldino, E., Casalbone, P., Felsani, A., Vescovi, A.L., Maira, G., and Mangiola, A. (2014). PDGF receptor α inhibition induces apoptosis in glioblastoma cancer stem cells refractory to anti-Notch and anti-EGFR treatment. *Mol. Cancer* 13, 247.

- Chen, J., Li, Y., Yu, T.-S., McKay, R.M., Burns, D.K., Kernie, S.G., and Parada, L.F. (2012). A restricted cell population propagates glioblastoma growth after chemotherapy. *Nature* 488, 522–526.
- Codega, P., Silva-Vargas, V., Paul, A., Maldonado-Soto, A.R., Deleo, A.M., Pastrana, E., and Doetsch, F. (2014). Prospective identification and purification of quiescent adult neural stem cells from their in vivo niche. *Neuron* 82, 545–559.
- De Santa, F., Totaro, M.G., Prosperini, E., Notarbartolo, S., Testa, G., and Natoli, G. (2007). The histone H3 lysine-27 demethylase Jmjd3 links inflammation to inhibition of polycomb-mediated gene silencing. *Cell* 130, 1083–1094.
- Dewaele, B., Wasag, B., Cools, J., Sciort, R., Prenen, H., Vandenberghe, P., Wozniak, A., Schöffski, P., Marynen, P., and Debiec-Rychter, M. (2008). Activity of dasatinib, a dual SRC/ABL kinase inhibitor, and IPI-504, a heat shock protein 90 inhibitor, against gastrointestinal stromal tumor-associated PDGFRAD842V mutation. *Clin. Cancer Res.* 14, 5749–5758.
- Doench, J.G., Hartenian, E., Graham, D.B., Tothova, Z., Hegde, M., Smith, I., Sullender, M., Ebert, B.L., Xavier, R.J., and Root, D.E. (2014). Rational design of highly active sgRNAs for CRISPR-Cas9-mediated gene inactivation. *Nat. Biotechnol.* 32, 1262–1267.
- Easwaran, H., Tsai, H.-C., and Baylin, S.B. (2014). Cancer epigenetics: tumor heterogeneity, plasticity of stem-like states, and drug resistance. *Mol. Cell* 54, 716–727.
- Eder, K., and Kalman, B. (2014). Molecular heterogeneity of glioblastoma and its clinical relevance. *Pathol. Oncol. Res.* 20, 777–787.
- ENCODE Project Consortium (2012). An integrated encyclopedia of DNA elements in the human genome. *Nature* 489, 57–74.
- Ene, C.I., Edwards, L., Riddick, G., Baysan, M., Woolard, K., Kotliarova, S., Lai, C., Belova, G., Cam, M., Walling, J., et al. (2012). Histone demethylase Jumonji D3 (JMJD3) as a tumor suppressor by regulating p53 protein nuclear stabilization. *PLoS ONE* 7, e51407.
- Gangemi, R.M.R., Griffero, F., Marubbi, D., Perera, M., Capra, M.C., Malatesta, P., Ravetti, G.L., Zona, G.L., Daga, A., and Corte, G. (2009). SOX2 silencing in glioblastoma tumor-initiating cells causes stop of proliferation and loss of tumorigenicity. *Stem Cells* 27, 40–48.
- Giachino, C., Boulay, J.-L., Ivanek, R., Alvarado, A., Tostado, C., Lugert, S., Tchorz, J., Coban, M., Mariani, L., Bettler, B., et al. (2015). A tumor suppressor function for Notch signaling in forebrain tumor subtypes. *Cancer Cell* 28, 730–742.
- GTEx Consortium (2013). The genotype-tissue expression (GTEx) project. *Nat. Genet.* 45, 580–585.
- Hashizume, R., Andor, N., Ihara, Y., Lerner, R., Gan, H., Chen, X., Fang, D., Huang, X., Tom, M.W., Ngo, V., et al. (2014). Pharmacologic inhibition of histone demethylation as a therapy for pediatric brainstem glioma. *Nat. Med.* 20, 1394–1396.
- Heinemann, B., Nielsen, J.M., Hudlebusch, H.R., Lees, M.J., Larsen, D.V., Boesen, T., Labelle, M., Gerlach, L.-O., Birk, P., and Helin, K. (2014). Inhibition of demethylases by GSK-J1/J4. *Nature* 514, E1–E2.
- Heinz, S., Benner, C., Spann, N., Bertolino, E., Lin, Y.C., Laslo, P., Cheng, J.X., Murre, C., Singh, H., and Glass, C.K. (2010). Simple combinations of lineage-determining transcription factors prime *cis*-regulatory elements required for macrophage and B cell identities. *Mol. Cell* 38, 576–589.
- Hulleman, E., Quarto, M., Vernell, R., Masserdotti, G., Colli, E., Kros, J.M., Levi, D., Gaetani, P., Tunic, P., Finocchiaro, G., et al. (2009). A role for the transcription factor HEY1 in glioblastoma. *J. Cell. Mol. Med.* 13, 136–146.
- Ikushima, H., Todo, T., Ino, Y., Takahashi, M., Miyazawa, K., and Miyazono, K. (2009). Autocrine TGF- β signaling maintains tumorigenicity of glioma-initiating cells through Sry-related HMG-box factors. *Cell Stem Cell* 5, 504–514.
- Imayoshi, I., and Kageyama, R. (2011). The role of Notch signaling in adult neurogenesis. *Mol. Neurobiol.* 44, 7–12.
- Imayoshi, I., Sakamoto, M., Yamaguchi, M., Mori, K., and Kageyama, R. (2010). Essential roles of Notch signaling in maintenance of neural stem cells in developing and adult brains. *J. Neurosci.* 30, 3489–3498.
- Johansson, C., Velupillai, S., Tumber, A., Szykowska, A., Hookway, E.S., Nowak, R.P., Strain-Damerell, C., Gileadi, C., Philpott, M., Burgess-Brown, N., et al. (2016). Structural analysis of human KDM5B guides histone demethylase inhibitor development. *Nat. Chem. Biol.* 12, 539–545.
- Knoechel, B., Roderick, J.E., Williamson, K.E., Zhu, J., Lohr, J.G., Cotton, M.J., Gillespie, S.M., Fernandez, D., Ku, M., Wang, H., et al. (2014). An epigenetic mechanism of resistance to targeted therapy in T cell acute lymphoblastic leukemia. *Nat. Genet.* 46, 364–370.
- Kopan, R., and Ilagan, M.X.G. (2009). The canonical Notch signaling pathway: unfolding the activation mechanism. *Cell* 137, 216–233.
- Koppikar, P., Bhagwat, N., Kilpivaara, O., Manshouri, T., Adli, M., Hricik, T., Liu, F., Saunders, L.M., Mullally, A., Abdel-Wahab, O., et al. (2012). Heterodimeric JAK-STAT activation as a mechanism of persistence to JAK2 inhibitor therapy. *Nature* 489, 155–159.
- Kovall, R.A., and Blacklow, S.C. (2010). Mechanistic insights into Notch receptor signaling from structural and biochemical studies. *Curr. Top. Dev. Biol.* 92, 31–71.
- Kruidenier, L., Chung, C.-W., Cheng, Z., Liddle, J., Che, K., Joberty, G., Bantscheff, M., Bountra, C., Bridges, A., Diallo, H., et al. (2012). A selective jumoni H3K27 demethylase inhibitor modulates the proinflammatory macrophage response. *Nature* 488, 404–408.
- Langmead, B., Trapnell, C., Pop, M., and Salzberg, S.L. (2009). Ultrafast and memory-efficient alignment of short DNA sequences to the human genome. *Genome Biol.* 10, R25.
- Lathia, J.D., Mack, S.C., Mulkearns-Hubert, E.E., Valentim, C.L.L., and Rich, J.N. (2015). Cancer stem cells in glioblastoma. *Genes Dev.* 29, 1203–1217.
- Lawrence, M., Huber, W., Pagès, H., Aboyoun, P., Carlson, M., Gentleman, R., Morgan, M.T., and Carey, V.J. (2013). Software for computing and annotating genomic ranges. *PLoS Comput. Biol.* 9, e1003118.
- Lee, J., Kotliarova, S., Kotliarov, Y., Li, A., Su, Q., Donin, N.M., Pastorino, S., Purow, B.W., Christopher, N., Zhang, W., et al. (2006). Tumor stem cells derived from glioblastomas cultured in bFGF and EGF more closely mirror the phenotype and genotype of primary tumors than do serum-cultured cell lines. *Cancer Cell* 9, 391–403.
- Leng, N., Li, Y., McIntosh, B.E., Nguyen, B.K., Duffin, B., Tian, S., Thomson, J.A., Dewey, C.N., Stewart, R., and Kendziorski, C. (2015). EBSeq-HMM: a Bayesian approach for identifying gene-expression changes in ordered RNA-seq experiments. *Bioinformatics* 31, 2614–2622.
- Li, B., and Dewey, C.N. (2011). RSEM: accurate transcript quantification from RNA-Seq data with or without a reference genome. *BMC Bioinformatics* 12, 323.
- Li, H., and Durbin, R. (2009). Fast and accurate short read alignment with Burrows-Wheeler transform. *Bioinformatics* 25, 1754–1760.
- Llorens-Bobadilla, E., Zhao, S., Baser, A., Saiz-Castro, G., Zwadlo, K., and Martin-Villalba, A. (2015). Single-cell transcriptomics reveals a population of dormant neural stem cells that become activated upon brain injury. *Cell Stem Cell* 17, 329–340.
- Louis, D.N., Ohgaki, H., Wiestler, O.D., and Cavenee, W.K. (2016). WHO Classification of Tumors of the Central Nervous System, Revised Fourth Edition (International Agency for Research on Cancer).
- Maillard, I., Weng, A.P., Carpenter, A.C., Rodriguez, C.G., Sai, H., Xu, L., Allman, D., Aster, J.C., and Pear, W.S. (2004). Mastermind critically regulates Notch-mediated lymphoid cell fate decisions. *Blood* 104, 1696–1702.
- Martynoga, B., Mateo, J.L., Zhou, B., Andersen, J., Achimastou, A., Urbán, N., van den Berg, D., Georgopoulou, D., Hadjir, S., Wittbrodt, J., et al. (2013). Epigenomic enhancer annotation reveals a key role for NF1X in neural stem cell quiescence. *Genes Dev.* 27, 1769–1786.
- McLendon, R., Friedman, A., Bigner, D., Van Meir, E.G., Brat, D.J.M., Mastrogiannis, G., Olson, J.J., Mikkelsen, T., Lehman, N., Aldape, K., et al.; Cancer Genome Atlas Research Network (2008). Comprehensive genomic characterization defines human glioblastoma genes and core pathways. *Nature* 455, 1061–1068.
- Mehta, S., Huillard, E., Kesari, S., Maire, C.L., Golebiowski, D., Harrington, E.P., Alberta, J.A., Kane, M.F., Theisen, M., Ligon, K.L., et al. (2011). The

- central nervous system-restricted transcription factor Olig2 opposes p53 responses to genotoxic damage in neural progenitors and malignant glioma. *Cancer Cell* 19, 359–371.
- Mizutani, K., Yoon, K., Dang, L., Tokunaga, A., and Gaiano, N. (2007). Differential Notch signalling distinguishes neural stem cells from intermediate progenitors. *Nature* 449, 351–355.
- Nathanson, D.A., Gini, B., Mottahedeh, J., Visnyei, K., Koga, T., Gomez, G., Eskin, A., Hwang, K., Wang, J., Masui, K., et al. (2014). Targeted therapy resistance mediated by dynamic regulation of extrachromosomal mutant EGFR DNA. *Science* 343, 72–76.
- Ntziachristos, P., Tsirigos, A., Welstead, G.G., Trimarchi, T., Bakogianni, S., Xu, L., Loizou, E., Holmfeldt, L., Strikoudis, A., King, B., et al. (2014). Contrasting roles of histone 3 lysine 27 demethylases in acute lymphoblastic leukaemia. *Nature* 514, 513–517.
- Paik, J.-H., Ding, Z., Narurkar, R., Ramkissoon, S., Muller, F., Kamoun, W.S., Chae, S.-S., Zheng, H., Ying, H., Mahoney, J., et al. (2009). FoxOs cooperatively regulate diverse pathways governing neural stem cell homeostasis. *Cell Stem Cell* 5, 540–553.
- Patel, A.P., Tirosh, I., Trombetta, J.J., Shalek, A.K., Gillespie, S.M., Wakimoto, H., Cahill, D.P., Nahed, B.V., Curry, W.T., Martuza, R.L., et al. (2014). Single-cell RNA-seq highlights intratumoral heterogeneity in primary glioblastoma. *Science* 344, 1396–1401.
- Picelli, S., Faridani, O.R., Björklund, A.K., Winberg, G., Sagasser, S., and Sandberg, R. (2014). Full-length RNA-seq from single cells using Smart-seq2. *Nat. Protoc.* 9, 171–181.
- R Core Team (2014). R: A language and environment for statistical computing. R Foundation for Statistical Computing (Austria: Vienna).
- Renault, V.M., Rafalski, V.A., Morgan, A.A., Salih, D.A.M., Brett, J.O., Webb, A.E., Villeda, S.A., Thekkat, P.U., Guillerey, C., Denko, N.C., et al. (2009). FoxO3 regulates neural stem cell homeostasis. *Cell Stem Cell* 5, 527–539.
- Rheinbay, E., Suvà, M.L., Gillespie, S.M., Wakimoto, H., Patel, A.P., Shahid, M., Oksuz, O., Rabkin, S.D., Martuza, R.L., Rivera, M.N., et al. (2013). An aberrant transcription factor network essential for Wnt signaling and stem cell maintenance in glioblastoma. *Cell Rep.* 3, 1567–1579.
- Roesch, A., Fukunaga-Kalabis, M., Schmidt, E.C., Zabierowski, S.E., Brafford, P.A., Vultur, A., Basu, D., Gimotty, P., Vogt, T., and Herlyn, M. (2010). A temporally distinct subpopulation of slow-cycling melanoma cells is required for continuous tumor growth. *Cell* 141, 583–594.
- Roesch, A., Vultur, A., Bogeski, I., Wang, H., Zimmermann, K.M., Speicher, D., Körbel, C., Laschke, M.W., Gimotty, P.A., Philipp, S.E., et al. (2013). Overcoming intrinsic multidrug resistance in melanoma by blocking the mitochondrial respiratory chain of slow-cycling JARID1B(high) cells. *Cancer Cell* 23, 811–825.
- Sharma, S.V., Lee, D.Y., Li, B., Quinlan, M.P., Takahashi, F., Maheswaran, S., McDermott, U., Azizian, N., Zou, L., Fischbach, M.A., et al. (2010). A chromatin-mediated reversible drug-tolerant state in cancer cell subpopulations. *Cell* 141, 69–80.
- Shen, L., Shao, N., Liu, X., and Nestler, E. (2014). Ngs.plot: quick mining and visualization of next-generation sequencing data by integrating genomic databases. *BMC Genomics* 15, 284.
- Shi, J., Wang, E., Milazzo, J.P., Wang, Z., Kinney, J.B., and Vakoc, C.R. (2015). Discovery of cancer drug targets by CRISPR-Cas9 screening of protein domains. *Nat. Biotechnol.* 33, 661–667.
- Simon, J.A., and Kingston, R.E. (2013). Occupying chromatin: oolycomb mechanisms for getting to genomic targets, stopping transcriptional traffic, and staying put. *Mol. Cell* 49, 808–824.
- Singh, S.K., Hawkins, C., Clarke, I.D., Squire, J.A., Bayani, J., Hide, T., Henkelman, R.M., Cusimano, M.D., and Dirks, P.B. (2004). Identification of human brain tumour initiating cells. *Nature* 429, 396–401.
- Son, M.J., Woolard, K., Nam, D.-H., Lee, J., and Fine, H.A. (2009). SSEA-1 is an enrichment marker for tumor-initiating cells in human glioblastoma. *Cell Stem Cell* 4, 440–452.
- Sosa, M.S., Bragado, P., and Aguirre-Ghiso, J.A. (2014). Mechanisms of disseminated cancer cell dormancy: an awakening field. *Nat. Rev. Cancer* 14, 611–622.
- Subramanian, A., Tamayo, P., Mootha, V.K., Mukherjee, S., Ebert, B.L., Gillette, M.A., Paulovich, A., Pomeroy, S.L., Golub, T.R., Lander, E.S., and Mesirov, J.P. (2005). Gene set enrichment analysis: a knowledge-based approach for interpreting genome-wide expression profiles. *Proc. Natl. Acad. Sci. USA* 102, 15545–15550.
- Suvà, M.L., Rheinbay, E., Gillespie, S.M., Patel, A.P., Wakimoto, H., Rabkin, S.D., Riggi, N., Chi, A.S., Cahill, D.P., Nahed, B.V., et al. (2014). Reconstructing and reprogramming the tumor-propagating potential of glioblastoma stem-like cells. *Cell* 157, 580–594.
- Tamura, K., Aoyagi, M., Ando, N., Ogishima, T., Wakimoto, H., Yamamoto, M., and Ohno, K. (2013). Expansion of CD133-positive glioma cells in recurrent de novo glioblastomas after radiotherapy and chemotherapy. *J. Neurosurg.* 119, 1145–1155.
- Tanaka, S., Louis, D.N., Curry, W.T., Batchelor, T.T., and Dietrich, J. (2013). Diagnostic and therapeutic avenues for glioblastoma: no longer a dead end? *Nat. Rev. Clin. Oncol.* 10, 14–26.
- Vanner, R.J., Remke, M., Gallo, M., Selvadurai, H.J., Coutinho, F., Lee, L., Kushida, M., Head, R., Morrissy, S., Zhu, X., et al. (2014). Quiescent sox2(+) cells drive hierarchical growth and relapse in sonic hedgehog subgroup medulloblastoma. *Cancer Cell* 26, 33–47.
- Verhaak, R.G.W., Hoadley, K.A., Purdom, E., Wang, V., Qi, Y., Wilkerson, M.D., Miller, C.R., Ding, L., Golub, T., Mesirov, J.P., et al.; Cancer Genome Atlas Research Network (2010). Integrated genomic analysis identifies clinically relevant subtypes of glioblastoma characterized by abnormalities in PDGFRA, IDH1, EGFR, and NF1. *Cancer Cell* 17, 98–110.
- Wakimoto, H., Kesari, S., Farrell, C.J., Curry, W.T., Jr., Zaupa, C., Agbi, M., Kuroda, T., Stemmer-Rachamimov, A., Shah, K., Liu, T.-C., et al. (2009). Human glioblastoma-derived cancer stem cells: establishment of invasive glioma models and treatment with oncolytic herpes simplex virus vectors. *Cancer Res.* 69, 3472–3481.
- Wang, H., Zou, J., Zhao, B., Johannsen, E., Ashworth, T., Wong, H., Pear, W.S., Schug, J., Blacklow, S.C., Arnett, K.L., et al. (2011). Genome-wide analysis reveals conserved and divergent features of Notch1/RBPJ binding in human and murine T-lymphoblastic leukemia cells. *Proc. Natl. Acad. Sci. USA* 108, 14908–14913.
- Wickham, H. (2009). Ggplot2: Elegant Graphics for Data Analysis, First Edition (Springer).
- Williams, K., Christensen, J., Rappilber, J., Nielsen, A.L., Johansen, J.V., and Helin, K. (2014). The histone lysine demethylase JMJD3/KDM6B is recruited to p53 bound promoters and enhancer elements in a p53 dependent manner. *PLoS ONE* 9, e96545.
- Xia, X., Lemieux, M.E., Li, W., Carroll, J.S., Brown, M., Liu, X.S., and Kung, A.L. (2009). Integrative analysis of HIF binding and transactivation reveals its role in maintaining histone methylation homeostasis. *Proc. Natl. Acad. Sci. USA* 106, 4260–4265.
- Xu, R., Shimizu, F., Hovinga, K., Beal, K., Karimi, S., Droms, L., Peck, K.K., Gutin, P., Iorgulescu, J.B., Kaley, T., et al. (2016). Molecular and clinical effects of Notch inhibition in glioma patients: a phase 0/1 trial. *Clin. Cancer Res.* 22, 4786–4796.
- Yahyanejad, S., King, H., Iglesias, V.S., Granton, P.V., Barbeau, L.M.O., van Hoof, S.J., Groot, A.J., Habets, R., Prickaerts, J., Chalmers, A.J., et al. (2016). NOTCH blockade combined with radiation therapy and temozolomide prolongs survival of orthotopic glioblastoma. *Oncotarget*. Published online May 10, 2016. <http://dx.doi.org/10.18632/oncotarget.9275>.
- Zhu, J., Adli, M., Zou, J.Y., Verstappen, G., Coyne, M., Zhang, X., Durham, T., Miri, M., Deshpande, V., De Jager, P.L., et al. (2013). Genome-wide chromatin state transitions associated with developmental and environmental cues. *Cell* 152, 642–654.
- Zhu, L.J., Gazin, C., Lawson, N.D., Pagès, H., Lin, S.M., Lapointe, D.S., and Green, M.R. (2010). ChIPpeakAnno: a bioconductor package to annotate ChIP-seq and ChIP-chip data. *BMC Bioinformatics* 11, 237.

STAR★METHODS

KEY RESOURCES TABLE

REAGENT or RESOURCE	SOURCE	IDENTIFIER
Antibodies		
EZH2	CST	Cat#5246
KDM6B	Abcam	Cat#ab38113; RRID:AB_943898
KDM5B	CST	Cat#3273
Cleaved Notch1 (Val1744)	CST	Cat#4147
Notch1	CST	Cat#3608
RBPJ	Abcam	Cat#Ab25949; RRID:AB_778155
Erk1/2 p44/p42	Millipore	Cat#05-1152; RRID:AB_1587015
Phosphor-Erk1/2 (Thr202/Tyr204, Thr185/Tyr187)	Millipore	Cat#05-797R; RRID:AB_1587016
Pan-Akt	CST	Cat#4060
phospho-PDGF Receptor α (Tyr849)/PDGF Receptor β (Tyr857)	CST	Cat#3170
PDGF Receptor α	CST	Cat#5241
β -Actin	Sigma-Aldrich	Cat#A5060; RRID:AB_476738
α -tubulin	Abcam	Cat#ab4074; RRID:AB_2288001
α -tubulin	CST	Cat#3873
Ki67 clone B56	BD Biosciences	Cat#558615; RRID:AB_647130
CD133/1 (AC133)	Miltenyi Biotec	Cat#130-098-829
PDGF Receptor α 16A1	BioLegend	Cat#323505; RRID:AB_2252226
H3K4me3	Millipore	Cat#07-473; RRID:AB_1977252
H3K27me3	Millipore	Cat#07-449; RRID:AB_310624
H3K27ac	Active Motif	Cat#39133; RRID:AB_2561016
Chemicals, Peptides, and Recombinant Proteins		
Dasatinib	Selleck Chemicals	Cat#S1021
Crenolanib	Selleck Chemicals	Cat#S2730
Imatinib mesylate	Selleck Chemicals	Cat#S1026
PD0325901	Selleck Chemicals	Cat#S1036
Palbociclib	Selleck Chemicals	Cat#S1116
MK-2206	Selleck Chemicals	Cat#S1078
Temozolomide	Selleck Chemicals	Cat#S1237
BKM120	Selleck Chemicals	Cat#S2247
Dacomitinib	Selleck Chemicals	Cat#S2727
Gefitinib	Selleck Chemicals	Cat#S1025
GSKJ4	Tocris	Cat#4594
GSKJ5	Tocris	Cat#4689
KDM5-C70	Xcess Biosciences	Cat#M60192-2
Compound E	Enzo Life Sciences	Cat#ALX-270-415
Recombinant human EGF	R&D Systems	Cat#236-EG
Recombinant human FGF	R&D Systems	Cat#233-FB
Recombinant human PDGF-AA	Shenandoah Biotechnology	Cat#100-16
Recombinant human PDGF-BB	Shenandoah Biotechnology	Cat#100-18
Critical Commercial Assays		
CellTiter-Glo	Promega	Cat#G7572
Click-iT EdU Flow Cytometry Assay kit	Life Technologies	Cat#C10338

(Continued on next page)

Continued

REAGENT or RESOURCE	SOURCE	IDENTIFIER
RNeasy Kit	QIAGEN	Cat#74106
DNeasy Blood & Tissue Kit	QIAGEN	Cat#69504
SuperScript III First-Strand Synthesis SuperMix	Life Technologies	Cat#18080400
Surveyor Mutation Detection Kit	Integrated DNA Technologies	Cat#706020
Deposited Data		
Raw and analyzed data	This paper	GSE74557
Experimental Models: Cell Lines		
GSC4	MGH	Wakimoto et al., 2009
GSC8	MGH	Wakimoto et al., 2009
GSC26	MGH	Wakimoto et al., 2009
GSC87	MGH	Wakimoto et al., 2009
GSC114	MGH	Wakimoto et al., 2009
GSC125	MGH	Wakimoto et al., 2009
CW1691B	Case Western	Jeremy Rich Lab
CW2907	Case Western	Jeremy Rich Lab
CW3246	Case Western	Jeremy Rich Lab
Experimental Models: Organisms/Strains		
Recombinant DNA		
pInducer20 dnMAML-GFP	This paper	
pInducer20 PDGFRA D842V	This paper	
pInducer20 PDGFRA	This paper	
lentiCRISPR v1	Addgene	49535
pDONR221	ThermoFisher	12536017
pInducer20	Addgene	44012
MigR1-dnMAML-GFP	Aster Lab	Maillard et al., 2004
Notch1 intracellular domain-pcw107	Addgene	64621
pDONR223-PDGFRA M260I	Addgene	23892
PDGFRA shRNA C09	TRC	TRCN0000196928
PDGFRA shRNA C11	TRC	TRCN0000195132
PDGFRA shRNA D11	TRC	TRCN0000426196
PDGFRA shRNA D12	TRC	TRCN0000419988
Sequence-Based Reagents		
See Table S4 for DNA primers used in this study	This paper	
Software and Algorithms		
ImageJ	NIH	https://imagej.nih.gov/ij/
Bowtie	Langmead et al., 2009	http://bowtie-bio.sourceforge.net/index.shtml
BWA	Li and Durbin, 2009	https://github.com/lh3/bwa
RSEM	Li and Dewey, 2011	https://www.biostat.wisc.edu/~cdewey/software.html
ngs.plot	Shen et al., 2014	https://github.com/shenlab-sinai/ngsplot
R statistical programming language	R Core Team, 2014	https://www.r-project.org/
Bioconductor	Core team	https://www.bioconductor.org/
HOMER	Heinz et al., 2010	http://homer.salk.edu/homer/

CONTACT FOR REAGENT AND RESOURCE SHARING

Further information and requests for reagents may be directed to, and will be fulfilled by, the Lead Contact Bradley Bernstein (bernstein.bradley@mgh.harvard.edu).

EXPERIMENTAL MODEL AND SUBJECT DETAILS

GSC Derivation and Cell Culture

Patient-derived GBM culture lines were obtained from Massachusetts General Hospital (GSC4, GSC8, GSC26, GSC87, GSC114, GSC125) (Wakimoto et. al 2009) and Case Western Reserve University (CW1691, CW2907, CW3246). For CW1691, CW2907 and CW3246, GBM tissues were obtained from excess surgical materials from patients after review from a neuropathologist and used in accordance with an approved protocol by the Institutional Review Board at Cleveland Clinic 2559; GBM cells were derived immediately after dissociation of primary patient tumor (CW1691) or after transient xenograft passage (CW2907). GBM lines were maintained in Neurobasal medium (Life Technologies) supplemented with N2/B27, penicillin/streptomycin (Life Technologies), GlutaMAX (Life Technologies), recombinant human EGF (20 ng/mL, R & D systems), and recombinant human FGF2 (20 ng/mL, R & D systems). GSC114, GSC115, CW1691, CW2907, and CW3246 were additionally supplemented with recombinant human PDGF-AA and PDGF-BB (20 ng/mL each, Shenandoah Biotechnology). CW1691 was grown as adherent monolayers using laminin (5 μ g/mL Engelbreth-Holm-Swarm laminin, Sigma).

GSC Persisters

For drug persister studies, fresh inhibitor and media were replenished every 4-6 days to GSC cultures. For downstream studies (e.g., ChIP, immunoblot, gene expression), viable cells were enriched using Lympholyte (Cedarlane) to viability levels comparable to untreated cultures.

Primary Patient Specimens

Single cell RNA-seq data for MGH26, MGH30, and MGH31 was taken from prior published studies (Patel et. al. 2014). Slides for immunohistochemistry for these tumors were cut from archived blocks kept in the MGH pathology tumor bank under Partners Institutional Review Board Protocol 2011P002334. For MGH64 and MGH66, samples were acquired fresh at time of surgical resection at the Massachusetts General Hospital. Patients were consented preoperatively according to the Institutional Review Board Protocol 1999P008145.

METHOD DETAILS

Cell Growth Assays

Freshly dissociated single cell suspensions were plated (96-well) in triplicate or quadruplicate at 1,000 to 10,000 cells/well for testing. For 4 day growth assays, CellTiter-Glo (Promega) was added to wells and end point luminescence was measured (BioTek Synergy HTX Platerereader). For 12-15 day assays, 1 \times compound in media was added at day 4-5 and all wells were replated with fresh media and compound at day 8-10 before viability was measured at day 12-15. For each inhibitor, $n = 3-5$ replicates were used for each concentration, and each inhibitor was repeated in two to four independent experiments.

CRISPR-Cas9 and shRNA Experiments

CRISPR sgRNA sequences were designed according to Doench et. al. (Doench et al., 2014), selected to target the demethylase catalytic domain (Shi et al., 2015), and subcloned into lentiCRISPR v1. sgRNA targeting sequences are included in Table S4. Lentiviruses were produced using standard protocols. Briefly, CRISPR plasmids were cotransfected with GAG/POL and VSVG plasmids into 293T packaging cells using FuGENE HD (Promega) to produce virus. Viral supernatant was collected 72 hr after transfection and concentrated using Lenti-X Concentrator (Clontech) following the manufacturer's instructions. Approximately 1.25×10^6 adherently attached GSC cells (5 μ g/mL Engelbreth-Holm-Swarm laminin, Sigma) were infected with concentrated virus for 24 hr, and were selected 48 hr after infection with puromycin (GSC4, GSC8: 1 μ g/mL, GSC87: 2 μ g/mL, Life Technologies) for 4 days. After 4-5 days of recovery, cells were dissociated and plated (96-well) in triplicate or quadruplicate at 2,500 to 5,000 cells/well. Growth was normalized to cells plated on day zero using an ATP standard curve measured at each time point. Each experiment was repeated in two to four independent experiments. Efficiency of genome editing was assessed by PCR amplification (PCR SuperMix, Life Technologies) of 50 ng of genomic DNA using primer sets surrounding the sgRNA-targeted region (~800 to 1,000 bp), followed by subjection of the resultant PCR products to SURVEYOR analysis according to the manufacturer's protocol (Integrated DNA Technologies, 706020). PCR primers for SURVEYOR analysis are listed in Table S4. For shRNA knockdown experiments, the following lentiviral shRNAs were obtained from the RNAi Consortium in the pLKO.1 vector: PDGFRA (TRCN0000195132, TRCN0000196928, TRCN0000426196, TRCN0000419988) and GFP. Virus generation and growth testing for shRNA experiments followed essentially identical protocols outlined above except the growth assay was begun immediately after puromycin selection due to the immediacy of the phenotype. shRNA infection was performed in two biological replicates and the cell growth assay was performed with four replicates.

Overexpression Studies

The PDGFRA M260I ORF was PCR-amplified from p-DONR223-PDGFRA M260I using primers containing flanking Gateway attB sites and a stop codon, and then subcloned into p-DONR221. Site directed mutagenesis was performed using QuickChange Lightning Site-Directed Mutagenesis Kit according to the manufacturer's instructions to generate wild-type PDGFRA (I260M) and

PDGFRA D842V, which were subsequently subcloned into p-Inducer 20 (pIND20). Notch1 ICD ORF was PCR-amplified from Notch1 intracellular domain-pcw107 (Addgene, plasmid # 64621) using primers containing flanking Gateway attB sites and was subcloned into p-DONR221 and pIND20. dnMAML-GFP ORF was PCR-amplified from MigR1-dnMAML (Maillard et al., 2004) using primers containing flanking Gateway attB sites and was subcloned into p-DONR221 and pIND20. Virus production and infection of cells was carried out as described above, and GSCs were selected with G418 (500 μ g/mL) for at least 1 week. pIND20 PDGFRA wt/D842V infected cells were induced with doxycycline (dox, 1 μ g/mL) for at least 3 days before cell growth assays were performed. pIND20 dnMAML and pIND20 GFP infected GSC cells were induced with dox (1 μ g/mL) for 4 days before mixed in equal proportion with uninfected GSC cells. Dox induction and mixing was performed independently in triplicate. The ratio of GFP⁺ to GFP⁻ cells was measured by flow cytometry at the indicated time points. Experiment was performed in two biological replicates from the same pIND20 dnMAML and pIND20 GFP lines.

Flow Cytometric Analysis

For cell cycle analysis, $\sim 1 \times 10^6$ viable dissociated cells were plated and treated with 1 μ M EdU for 2 hr. Cells were then washed with PBS, incubated with Zombie Aqua viability dye (Biolegend) or Live/Dead fixable far red dead cell stain kit (Life Technologies) for 20 min, washed with PBS, and then fixed with ice-cold 70% ethanol. Staining for EdU was performed using the Click-iT EdU Flow Cytometry Assay kit (Life Technologies) according to the manufacturer's protocol. DNA content was visualized using FxCycle Violet (Life Technologies). Ki67 (clone B56, BD Biosciences) was stained for 30 min at ambient temperature. For surface marker analysis, cells were washed with PBS and stained with antibodies against CD15 (VIMC6, Miltenyi Biotec), CD133/1 (AC133, Miltenyi Biotec), or PDGFR α (16A1, BioLegend) for 30 min at 4°C. Gates were determined using an unstained control, where $\sim 2\%$ of cells were considered positive. All experiments were performed with at least two biological replicates.

Immunohistochemistry and Spectral Imaging of Primary GBM Specimens

Immunohistochemical staining of formalin-fixed, paraffin-embedded sections of four primary GBM specimens was done on a Leica Bond III automated workstation. Dual staining for activated NOTCH1 (N1ICD) and Ki67 was performed following antigen retrieval using Bond Epitope Retrieval 2 solution for 40 min. Slides were first incubated with antibody against N1ICD (D3B8, Cell Signaling Technology, 4147) at a 1:50 dilution for 60 min at ambient temperature, followed by incubation with a rabbit-specific secondary antibody linked to horseradish peroxidase (Bond Polymer Refine Detection kit). N1ICD staining was developed with diaminobenzidine (Leica Detection kit). Slides were then incubated with a mouse monoclonal antibody specific for Ki67 (8D5) at a 1:8,000 dilution for 30 min. Binding of anti-Ki67 was detected using the mouse-specific Bond Polymer Refine Red Detection kit, which detects staining using Fast Red. Slides were then counterstained with hematoxylin, dehydrated, and coverslipped.

To generate spectral libraries, single-stained tissue sections were imaged using the Mantra multispectral imaging platform (PerkinElmer). The spectrally resolved individual profiles between 420–720 nm of 3,3'-diaminobenzidine (DAB; N1ICD), Fast Red (Ki67) and hematoxylin counterstain were used to deconvolute staining patterns in double-stained tissue sections. Five representative areas of each stained tissue section ($n = 2$ per patient sample) were imaged at 20 \times magnification and deconvoluted using the Inform 2.1 software package (PerkinElmer).

Immunoblotting

Cells were lysed on ice using RIPA buffer (50 mM Tris-HCl pH 7.5, 150 mM NaCl, 0.5% sodium deoxycholate, 1% NP-40, 0.1% SDS) supplemented with fresh protease (HALT, Thermofisher; PMSF, 1 mM) and phosphatase inhibitors (Thermofisher). After 30 min, benzamide was added with MgCl₂ (1 mM) to clarify the cell lysate. Immunoblotting was performed according to standard procedures.

Tumor Dissociation

MGH66 patient sample was confirmed to be glioblastoma by frozen section diagnosis at the time of resection. Tissue was minced into < 1mm pieces with a scalpel and enzymatically dissociated using the Brain Tumor Dissociation Kit (Miltenyi Biotec). Digested tissue was strained through a 100 micron cell strainer, washed in PBS and then layered carefully onto a 5mL density gradient (Lympholyte-H, Cedar Lane labs), which was centrifuged at 2,000 rpm for 10 min at room temperature. Dead cells, debris, and RBCs were pelleted and live cells collected from the interface and used for downstream applications including staining, flow cytometry, and single cell analysis. Viability was measured using trypan blue exclusion, which confirmed > 90% cell viability.

Fluorescence-activated cell sorting of primary tumors

Tumor cells were suspended in 1% bovine serum albumin in Hanks buffered saline solution (BSA / HBSS) for blocking, and stained first with CD45-Vioblu direct antibody conjugate (Miltenyi Biotec) for 30 min at 4°C. After washing in cold PBS, cells were resuspended in 1 mL of BSA/HBSS containing 1 μ M calcein AM (Life Technologies) and 0.33 μ M TO-PRO-3 iodide (Life Technologies) and stained for 30 min prior to cell sorting. Cells were run on a FACSria Fusion Special Order System (Becton Dickinson) using 488nm (calcein AM, 530/30 filter), 640nm (TO-PRO-3, 670/14 filter), and 405nm (Vioblu, 450/50 filter) lasers. Singlet gating was performed using strict forward scatter height versus area criteria to eliminate doublets. Viable cells were identified by staining positive with calcein AM but negative for TO-PRO-3. Single cells were sorted into 96-well plates containing cold buffer TCL buffer (QIAGEN) containing 1% β -mercaptoethanol, snap frozen on dry ice, and then stored at -80°C prior to whole transcriptome amplification, library preparation, and sequencing.

Single-cell whole transcriptome amplification, library construction, and sequencing

Libraries from isolated single cells were generated based on the Smart-seq2 protocol (Picelli et al., 2014) with the following modifications. Agencourt RNAClean XP beads (Beckman Coulter) were used to purify single cell RNA prior to oligo-dT primed reverse transcription with Maxima reverse transcriptase and locked TSO oligonucleotide. Amplification of cDNA libraries was done with 20 cycle PCR amplification using KAPA HiFi HotStart ReadyMix (KAPA Biosystems) with subsequent Agencourt AMPure XP bead purification as described. Library preparation by tagmentation was done using the Nextera XT Library Prep kit (Illumina) with custom barcode adapters (sequences available upon request). Libraries from 384 cells from MGH66 with unique barcodes were combined and sequenced using a NextSeq 500 sequencer (Illumina).

Real-Time Quantitative RT-PCR and RNA-seq Library Preparation

Whole RNA was extracted from $1-3 \times 10^6$ cells using the QIAGEN RNeasy kit according to the manufacturer's protocol. For qRT-PCR, total RNA was reverse-transcribed into cDNA (High Capacity cDNA Reverse Transcriptase Kit, Applied Biosystems) and qRT-PCR amplification was performed in triplicate using fast SYBR Green Master Mix (Life Technologies) with specific PCR primers for genes of interest and 18S as an endogenous control. qRT-PCR experiments were performed with two biological replicates. Relative quantification for each target was performed using the comparative Ct method (Applied Biosystems). Sequences for qRT-PCR primers used are listed in Table S4. For RNA-seq library preparation, Poly(A)⁺ RNA was enriched using magnetic oligo(dT)-beads (Life Technologies) and then ligated to RNA adaptors for sequencing. RNA-seq was performed with three biological replicates per GSC line and/or condition.

ChIP-seq

Briefly, formaldehyde-fixed cells were lysed and sheared (Branson S220) on wet ice. The sheared chromatin was cleared and incubated overnight at 4°C with the following antibodies: H3K4me3 (Millipore, 07-473, Lot 2207275), H3K27me3 (Millipore, 07-449, lot 2382150), H3K27ac (Active Motif, 39133 lot 25812006), RBPJ (Abcam, ab25949, lot GR169397-1), and cleaved Notch1 (CST, 4147, lot #4). Antibody-chromatin complexes were immunoprecipitated with protein G magnetic Dynal beads (Life Technologies), washed, eluted, reverse crosslinked, and treated with RNase A followed by proteinase K. ChIP DNA was purified using Ampure XP beads (Beckmann Coulter) and then used to prepare sequencing libraries for sequencing with the Next-Seq Illumina genome analyzer. Experiments were performed once.

QUANTIFICATION AND STATISTICAL ANALYSIS

Statistical parameters including the exact value of *n*, the definition of center, dispersion, and precision measures (mean ± SD or SEM) and statistical significance are reported in Figures and Figure Legends, as well as below. As a general rule, we considered data to be statistically significant when *p* < 0.05 by two-tailed Student's T-Test, Wilcoxon rank-sum test or a Friedman test where appropriate.

Levels phosphorylated PDGFR α , Akt, and Erk1/2

For each assay *n* = 2 biological replicates involving separate drug treatments.

Cell growth assays (Cell-titer Glo)

N = 3-4 replicates per cell line. *N* = 2-4 independent experiments per compound, and 3-5 replicates per concentration (see figure legends for more detail). For overexpression studies *n* = 2. Relative CTG (Cell-tier Glo) values were normalized to *T*₀ (y axis) over a time course (x axis) following treatment. Error was calculated as either s.d or s.e.m across all biological replicates. IC₅₀ values: Calculated as standard, from at least three biological replicates.

CRISPR-Cas9 and shRNA experiments

Each CRISPR-Cas9 sgRNA experiment was repeated in two to four independent experiments involving separate infections; in each experiment, cells were plated in *n* = 3-5 replicates for the cell growth assay. shRNA infection was performed in two biological replicates and the cell growth assay was performed with *n* = 4 replicates. Growth was normalized to cells plated on day zero using an ATP standard curve measured at each time point.

Overexpression studies

Dox induction and mixing was performed independently in triplicate. The ratio of GFP⁺ to GFP⁻ cells was measured by flow cytometry at the indicated time points, and error bars were calculated as s.e.m. across all three biological replicates (indicated in the figure legends). Experiment was performed in two biological replicates from the same pIND20 dnMAML and pIND20 GFP lines.

Flow Cytometric Analysis

PDGFR α staining was performed with two biological replicates, while staining for CD133 and CD15 were performed with three biological replicates. Gates were determined using an unstained control, where ~2% of cells were considered positive. Error bars

were calculated as s.e.m. across three replicates and significance was determined using a two-tailed Student's T-Test. Cell cycle analysis was performed with at least three biological replicates per time point, and gates were determined for each time point by the relative proportions of DAPI and EdU labeling.

Immunohistochemistry and Spectral Imaging of Primary GBM Specimens

Single slides from four tumors were stained with antibodies against Notch1 and Ki67 (see above methods) in two separate replicates. From each slide, five representative regions were quantified using spectral imaging, yielding > 10,000 cells quantified per sample over two replicates.

Single-cell RNA-seq data analysis

Libraries from 384 cells from a single tumor (MGH66) were combined and sequenced. Paired-end, 38-base reads were mapped using Bowtie (Langmead et al., 2009) with parameters “-q-phred33-quals -n 1 -e 99999999 -l 25 -l 1 -X 2000 -a -m 15 -S -p 6” to the UCSC hg19 human transcriptome, which permits alignment of sequences with single base changes to account for point mutations. RSEM v1.2.3 (Li and Dewey, 2011) in paired end mode using parameters “-estimate-rspd-paired-end -sam -p 6” was used to quantify expression in the form of normalized transcripts per million (TPM) for each gene in each single cell. Data for tumors MGH26, MGH28, and MGH30 were prepared as previously published in (Patel et al., 2014).

To remove low quality data for each tumor, we excluded all cells with less than 3,000 detectable genes and all genes with a mean TPM less than 10. The TPM values were subjected to base 2 logarithmic transformation after adding 1 to each value to avoid singularities. To account for global mean expression differences across cells, for each cell a size factor was calculated as described in (Anders and Huber, 2010) with the following modifications: i) computations were performed in log-space and adjusted accordingly; ii) the mean over all genes as opposed to the median was used ultimately. The cell-specific size factors were subtracted from the transformed TPM values. To assess the cell cycle state we used the cell cycle signature derived in our previous study (see (Patel et al., 2014) for details). To score single-cells for individual signatures (e.g., cell cycle or persister signatures) we computed mean TPM values for the corresponding signature gene sets and transformed resulting values into standard scores (z-scores). Gene signatures used are listed in Table S3.

Population RNA-seq analysis

Paired-end reads were aligned to UCSC transcriptome (hg19) using Bowtie (Langmead et al., 2009) (version 0.12.7) with the following parameters: -chunkmbs 512 -q-phred33-quals -n 0 -l 25 -l 1 -X 2000 -p 6 -a -m 15. Gene expression, quantified as transcript per million (TPM), was estimated using RSEM (Li and Dewey, 2011) with the following parameters: -fragment-length-max 1000-estimate-rspd-paired-end.

Data processing was performed using R version $\geq 3.1.0$ (<http://survey-winner.net>) and BioConductor (<http://www.bioconductor.org>). All heatmaps were generated using the R package ggplot2 (Wickham 2009). To identify variable genes across the time course of drug treatment, triplicate RNA-seq datasets were generated for each time point and processed as outlined above. The resulting TPM values were employed for differential gene expression analysis using the R package EBSeq (Leng et al., 2015). To identify variable genes the following pairwise comparisons were performed: GSC8 naive versus GSC8^{12d}, GSC8 naive versus GSC8^{Per}, GSC8^{12d} versus GSC8^{Per}. We considered all genes with a posterior probability of differential expression (PPDE) greater than 0.5 in at least one of the comparisons as variable genes. A table of all genes and significantly differentially expressed genes is provided in Table S2. GSEA version 2.1 (Subramanian et al., 2005) was carried out using signal-to-noise on log₂ + 1 transformed TPM values as the metric; genes with mean TPM less than 10 under all given conditions were excluded from analysis. Gene signatures used for GSEA are listed in Table S3. For the comparison with GTEx expression data (GTEx Consortium, 2013), RPKM values were computed.

ChIP-seq data analysis

All experiments were performed once. Reads were aligned to hg19 using BWA (Li and Durbin, 2009) and identical ChIP-seq sequence reads were collapsed to avoid PCR duplicates. In order to avoid possible saturation biases, reads were downsampled to approximately similar numbers (~20 million reads). Peaks were called using HOMER v4.6 (Heinz et al., 2010) using matched inputs with the following parameters: H3K4me3, -histone -tagThreshold 30; H3K27ac, -histone -tagThreshold 50; H3K27me3, -histone -size 3000 -minDist 2500 -F 1.5 -L 0 -FDR 0.1; Notch1 ICD, -factor; and RBPJ, -factor. TF motif enrichment analysis was performed using HOMER v4.6 on 1 kb windows centered on previously called H3K27ac, Notch1 ICD, and RBPJ peaks (parameters: -size given -mask) and p values presented were provided by the software. Quantification of the H3K27me3 ChIP-seq signals, using fore- and background normalization, was essentially performed as outlined in (Zhu et al., 2013) with few modifications. To exclude genomic regions with potential copy number aberrations, we quantified read counts derived from whole cell extracts ChIP-seq within 5 kb genomic windows. Read counts were performed using the R package GenomicRanges (Lawrence et al., 2013). To compute normalization constants, all genomic windows with read counts equal to 0 or greater than 3 standard deviations from the mean were excluded from the analysis. For a given H3K27me3 ChIP-seq dataset, the background constant was estimated as the median of the read count distribution within 5 kb windows overlapping the 5% most highly expressed genes, as active genes are considered to be devoid of repressive chromatin modifications. The foreground signal was estimated as the median of the read count distribution within 5 kb windows centered around each called peak and subtracting the background signal. To quantify H3K27me3 signal within 5 kb regions of interest, the background signal was subtracted from the corresponding read count and the resulting value divided by

the foreground signal. Values smaller or larger than 0 or 1 were mapped to 0 or 1, respectively. The fore- and background normalization of H3K27ac was performed analogously but with the following modifications. To account for the narrower signal, all operations were performed using 1 kb windows. For a given H3K27ac ChIP-seq dataset, the background signal was estimated as the median of the read count distribution within all 1 kb windows across the genome but not overlapping with a called peak. To account for greater dynamic range, the foreground signal was estimated as the 0.95-quantile of the read count distribution within 1 kb windows centered around each called peak and subtracting the background constant. To estimate the H3K27ac signal within a 1 kb region of interest, the background constant was subtracted from the corresponding read count and the resulting value was divided by the foreground constant. Values smaller or larger than 0 or 1 were mapped to 0 or 1, respectively. In order to quantify ChIP-seq intensities within genomic regions of different sizes (e.g., genes), the obtained normalization constants were scaled accordingly. Association of peaks with neighboring genes was performed using the R package ChIPpeakAnno (Zhu et al., 2010).

ChIP-seq Binding Profiles

ChIP-seq profile plots were generated using ngs.plot (Shen et al., 2014). To assess H3K27me3 levels across broad domains, H3K27me3 metaprofiles were generated over the union of peaks, called in each of the corresponding GSC8 persister conditions, and having a minimum size of 10 kb.

DATA AND SOFTWARE AVAILABILITY

The accession number for the gene expression and ChIP-seq data reported in this paper is NCBI GEO: GSE74557.